Measurement of Tagged Deep Inelastic Scattering (TDIS)

May 21, 2015

Hall A and SBS Collaboration Proposal

Dasuni Adikaram, Alexandre Camsonne, Dave Gaskell, Doug Higinbotham, Mark Jones, Cynthia Keppel (Spokesperson) [1], Wally Melnitchouk, Christian Weiss, Bogdan Wojtsekhowski (Spokesperson)
JEFFERSON LAB

John Arrington, Roy Holt, Sixue Qin, Paul Reimer, Craig Roberts
ARGONNE NATIONAL LAB

Paul King (Spokesperson), Julie Roche
OHIO UNIVERSITY

Krishna Adhikari, Jim Dunne, Dipangkar Dutta (Spokesperson), Lamiaa El-Fassi, and Li Ye
MISSISSIPPI STATE UNIVERSITY

Charles Hyde, Sebastian Kuhn, Lawrence Weinstein
OLD DOMINION UNIVERSITY

John Annand (Spokesperson), David Hamilton, Derek Glazier, Dave Ireland, Kenneth Livingston,
Ian MacGregor, Bryan McKinnon, Bjoern Seitz, Daria Sokhan
UNIVERSITY OF GLASGOW

Jen-Chieh Peng
UNIVERSITY OF ILLINOIS AT URBANA CHAMPAIGN

Gordon Cates, Kondo Gnanvo, Richard Lindgren, Nilanga Liyanage, Jixie Zhang (Spokesperson)
UNIVERSITY OF VIRGINIA

Todd Averett, Keith Griffeon
COLLEGE OF WILLIAM AND MARY

Tim Hobbs, Thomas Londergan
INDIANA UNIVERSITY

Xiaodong Jiang
LOS ALAMOS NATIONAL LABORATORY

Michael Christy, Narbe Kalantarians, Michael Kohl, Peter Monaghan, Liguang Tang
HAMPTON UNIVERSITY

Ioana Niculescu, Gabriel Niculescu
JAMES MADISON UNIVERSITY

Boris Kopeliovich, Nuruzzaman, I. Potashnikova
UNIVERSIDAD TECNICA FREDERICO SANTA MARIA

Andrew Puckett
UNIVERSITY OF CONNECTICUT

Garth Huber
UNIVERSITY OF REGINA

[1]Contact person

Abstract

We propose to investigate tagged deep inelastic scattering (TDIS) by measuring high W^2, Q^2 electrons scattered from hydrogen and deuterium targets in coincidence with low momentum recoiling protons. This is a pioneering experiment that will probe the elusive mesonic content of the nucleon, using the tagging technique to scatter for example from the pion in proton to pion fluctuations. This approach will also provide access to the pion structure function via the Sullivan process.

The experiment utilizes the Hall A Super BigBite spectrometer for electron detection, in conjunction with a low density target, and, a radial time projection chamber (RTPC) with GEM-based readout, inside a large diameter 5T solenoid. These combined systems, along with the CEBAF high current CW beam, leverage the high luminosity and unique kinematics required to access the proposed physics.

The low momentum tagging technique is crucial for the experimental separation of competing processes, leading to the isolation of the electron-meson scattering contribution. The $D(e, e'np)$ process will be used to calibrate the RTPC, allowing absolute TDIS cross section measurement. The low density target, as demonstrated in BONuS, will allow the use of an effective free neutron target, essential for the study of the virtual photon - charged meson interaction, which has significant advantage for theoretical interpretation. Complementary data on the neutral meson interaction will also be collected for the first time.

Contents

1 Physics Motivation

The concept of a composite nucleon structure may be tracked as far back as 1933 to the discovery of the anomalous magnetic moment of the proton [1]. This was explicitly formulated by Fermi and Marshall who noted in a 1947 paper [2] that experimental evidence pointed to the nucleon existing approximately 20% of the time in a virtual meson-nucleon state. The virtual meson "cloud" of the nucleon plays an important role in the understanding of the nucleon-nucleon interaction and the pion cloud in particular has always been considered critical to understanding the nucleon's long-range structure. At shorter ranges, the role of mesons in electron-nucleon deep inelastic scattering (DIS) have also been investigated. In 1972 Sullivan [3] suggested that some fraction of the nucleon's anti-quark sea distribution may be associated with this pion content of the nucleon. For many decades these and numerous other theories that describe and/or utilize the meson cloud of the nucleon have advanced significantly (see [4, 5, 6] for some review). From partially conserved axial current to the success of chiral quark models, it is considered known that the nucleon has an associated meson cloud. In very stark contrast to the substantial body of theory associated with the meson cloud, however, experimental results remain few and far between. In a 1983 paper, Thomas commented that "...it is rather disturbing that no one has yet provided direct experimental evidence of a pionic component in the nucleon" [7]. Even with results becoming available from Drell-Yan experiments at Fermilab, W production at RHIC, and diffractive DIS at HERA and COMPASS, all discussed below, the "disturbing" situation is not yet been substantially improved.

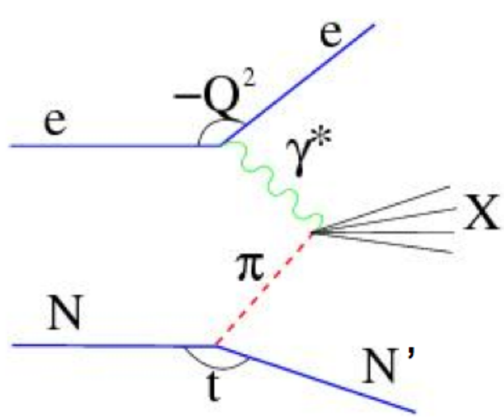

Figure 1: Feynman diagram for electron scattering from the pion cloud of the nucleon N, with the initial nucleon at rest (the Sullivan process).

The 12 GeV upgrade of JLab presents new opportunities to study the mesonic structure of the nucleon. One such technique is to measure the contribution to electron Deep Inelastic Scattering (DIS) off the meson cloud of a nucleon target, as pointed out by Sullivan [3] (Fig. 1). This so-called Sullivan process was shown to persist even at large Q^2 scales. An immediate consequence of the Sullivan process is that the nucleon parton distributions contain a component which can be attributed to the meson cloud. This intriguing idea remained untested for many years. In the early 1980s, Thomas [7] predicted several implications of the Sullivan process for nucleon parton distributions using a cloudy-bag model for describing the meson cloud. In particular, it was predicted that the nucleon sea should have an up/down sea-quark flavor asymmetry, as well as an s/$\bar{s}$ asymmetry for the strange quark sea. The earliest parton models assumed that the proton sea was flavor symmetric, even though the valence quark distributions are clearly flavor asymmetric. The assumption of flavor symmetry was not based on any known physics, and it remained untested by experiments. A direct method to check this assumption is to compare the sea in the neutron to that in the proton by measuring the Gottfried integral in DIS. The Gottfried Sum Rule (GSR) gives the following relation for the proton and neutron structure functions F_2^p and F_2^n:

$$I_{\text{GSR}} = \int_0^1 [F_2^p(x) - F_2^n(x)]/x dx = \frac{1}{3} + \frac{2}{3}\int_0^1 [\bar{u}(x) - \bar{d}(x)]dx = \frac{1}{3}. \quad (1)$$

In the early 1990s, the NMC collaboration reported [8] an observation of the violation of the GSR[9], $I_{\text{GSR}} = 0.235 \pm 0.026$. Since the GSR is derived under the assumption of $\bar{d}(x) = \bar{u}(x)$, the NMC result strongly suggests that this assumption is invalid. Indeed, Eq. 1 and the NMC result imply that

$$\int_0^1 (\bar{d}(x) - \bar{u}(x))dx = 0.148 \pm 0.039 \quad (2)$$

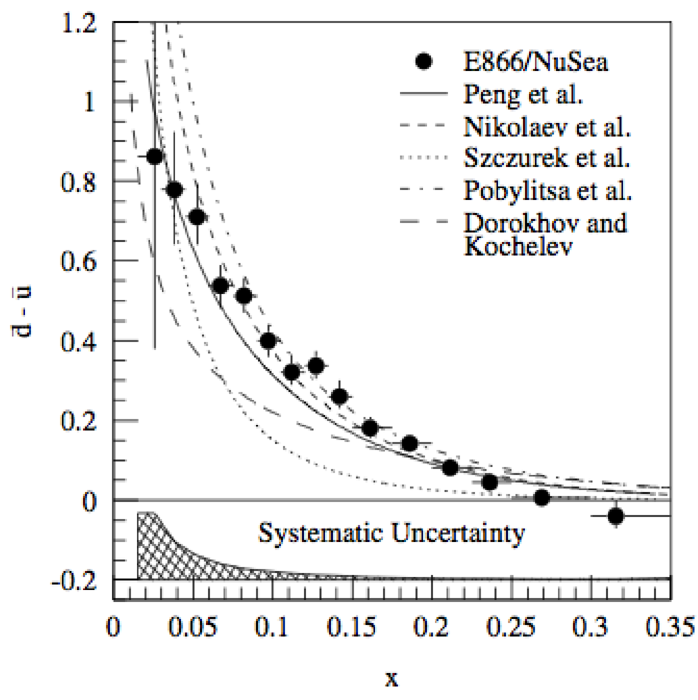

Figure 2: Comparison of the E866 $\bar{d}\bar{u}$ data with various model calculations [13]

Independent confirmation of the $\bar{d}/\bar{u}$ flavor asymmetry was later provided by Drell-Yan experiments [10, 11, 12, 13] and the semi-inclusive DIS experiment [14]. Figure 2 shows the E866 result on $\bar{d}(x) - \bar{u}(x)$ at $Q^2 = 54$ GeV$^2/c^2$. The surprisingly large asymmetry between $\bar{d}$ and $\bar{u}$ is observed over a broad range of x. The E866 data provide a direct evaluation of the $d-u$ integral, namely, $\int_0^1 (\bar{d}(x)\bar{u}(x))dx = 0.118 \pm 0.012$, which is in good agreement with the NMC result shown in Eq. 2. The observation of $\bar{u}$, $\bar{d}$ flavor asymmetry has inspired many theoretical works regarding the origin of this asymmetry. Perturbative QCD, in which the $q\bar{q}$ sea is generated from the $g \to q\bar{q}$ splitting, has difficulties explaining such an asymmetry. The small d, u mass difference (actually, $m_d > m_u$) of 2 to 4 MeV compared to the nucleon confinement scale of 200 MeV does not permit any appreciable difference in their relative production by gluons.

Regardless, one observes a surplus of $\bar{d}$ which is the heavier of the two species. Field and Feynman long time ago speculated that the $g \to u\bar{u}$ process would be suppressed relative to $g \to d\bar{d}$ due to a Pauli-blocking effect arising from the presence of two u-quarks as compared to a single d-quark in proton. The consequences of Pauli-blocking have, however, been shown to be small [15]. Thus, another, presumably non-perturbative, mechanism must account for the large measured $\bar{d}$, $\bar{u}$ asymmetry. Many of the non-perturbative approaches to explain the $\bar{d}$, $\bar{u}$ asymmetry involve the use of isovector mesons (particularly the pion). Recent reviews [16, 17, 18] have extensive discussions on various theoretical models. In the meson-cloud model, the virtual pion is emitted by the proton and the intermediate state is pion + baryon. More specifically, the proton is taken to be a linear combination of a "bare" proton plus pion-nucleon and pion-delta states, as below,

$$\begin{aligned} |p> \;\; &\to \;\; \sqrt{1-a-b}|p_0> + \sqrt{a}(-\sqrt{\frac{1}{3}}|p_0\pi^0> + \sqrt{\frac{2}{3}}|n_0\pi^+>) \\ &+\sqrt{b}(\sqrt{\frac{1}{2}}|\Delta_0^{+}\pi^-> - \sqrt{\frac{1}{3}}|\Delta_0^{+}\pi^0> + \sqrt{\frac{1}{6}}|\Delta_0^{0}\pi^+>) \end{aligned} \quad (3)$$

The subscript zeros on the virtual baryon states indicate that they are assumed to have symmetric seas, so the asymmetry in the antiquarks must be largely generated from the pion valence distribution. The coefficients a and b are the fractions of the πN and $\pi\Delta$ configurations, respectively, in the proton. These fractions can be calculated using the πNN and $\pi N\Delta$ couplings, and form factors may be obtained from experiment. The asymmetry in the proton sea then arises because of the dominance of π^+ among the virtual configurations. Figure 2 shows that the pion-cloud model can reproduce the x-dependence of the $\bar{d}\bar{u}$ distribution very well. The success of the meson-cloud model in explaining the $\bar{d}$, $\bar{u}$ asymmetry suggests that a direct measurement of the meson cloud in DIS, such as that proposed here, is feasible. The idea is that the meson cloud in the nucleon could be considered *as a virtual target* to be probed by various hard processes, including DIS.

We here propose to measure the semi-inclusive reactions $H(e, e'p)X$ and $D(e, e'pp)X$ in the deep inelastic regime of $8 < W^2 < 18$ GeV^2, $1 < Q^2 < 3$ GeV^2, and $0.05 < x < 0.2$, for very low proton momenta in the range 60 MeV/c up to 400 MeV/c. The key to this experimental technique is to measure the low-energy outgoing "recoil" proton in coincidence with a deeply inelastically scattered electron from the hydrogen target. In the deuterium case, an *additional* low energy spectator proton will be identified at backward angle to identify the neutron target. The inclusive electron kinematics determine that a DIS event has occurred, i.e. that the reconstructed Q^2 and missing mass, W^2, of the recoiling hadronic system are sufficiently large. However, unlike the standard inclusive case, the low momentum protons N' measured in time and vertex coincidence with the DIS event ensure that the deep inelastic scattering occurred from partons within the meson cloud (here identified as a pion) surrounding the nucleon. This can be achieved by employing the Super Bigbite Spectrometer to detect the scattered electrons in time and vertex coincidence with low momentum proton(s) measured in a low mass radial time projection chamber (RTPC, a BONUS experiment type detector).

The idea of considering the meson cloud as a virtual pion target was used at the HERA $e-p$ collider to measure the pion structure functions at low-x in a hard diffractive process, where forward-going neutrons or protons were tagged in coincidence with the DIS events, as shown in Fig. 1. While the HERA experiments have provided very interesting first data on the extraction of pion structure functions using the Sullivan process, there are many reasons for extending such measurements to JLab energies. The pion, being the lightest and simplest hadron, has a central role in our current description of nucleon and nuclear structure. The pion has been used to explain the long-range nucleon-nucleon interaction, making it a fundamental component of the Standard Model of Nuclear Physics [19, 20, 21]. The pion is also used to explain the flavor asymmetry of the quark sea in the nucleon. Moreover, the masses of light mesons such as the pion are believed to arise from dynamical chiral symmetry breaking [22], and thus models of the pion must account for both its role as the Goldstone boson of quantum chromodynamics (QCD) and as a quark-antiquark system.

Experimental knowledge of the partonic structure of the pion is very limited due to the lack of a stable pion target. Most of the current knowledge of the pion structure function in the valence region is obtained primarily from pionic Drell-Yan scattering [23]-[25], and in the pion sea region at low Bjorken-x, from hard diffractive processes measured on $e-p$ collisions at HERA [27]. The existing data on the pion structure function from Drell-Yan scattering is shown in Fig 3. Also shown, in Fig. 4, is the pion structure function data at low x from HERA, where forward-going neutrons or protons were tagged in coincidence with the DIS events. These results seem to indicate that the pion sea has approximately one-third of the magnitude of the proton sea, while from the parton model one expects the pion sea to be two-thirds of the proton sea.

There are several theoretical calculations of the pion structure in the valence region, however they tend to disagree with each other. The parton model [28], perturbative QCD based models [29, 30] and some non-perturbative models such as those based on the Dyson-Schwinger Equation [26]-[33] predict a $(1-x)^a$ dependence with $a \geq 2$. On the other hand relativistic constituent quark models [34, 35], Nambu-Jona-Lasinio models [36]-[39], the Drell-Yan-West relation [40, 41] and even arguments based on quark-hadron duality [42] favor a linear $(1-x)$ dependence of the pion structure function at high-x. Calculations of the pion structure function in the pion sea region, such as those of the chiral quark model [43], also disagree with the extraction from the HERA data, in fact these models predict that the momentum fraction of pion sea is larger than the proton sea. These discrepancies tell us that it is essential to measure the pion structure function over a wide range of x using new techniques.

The HERA kinematics are limited to the very low x region, where no independent

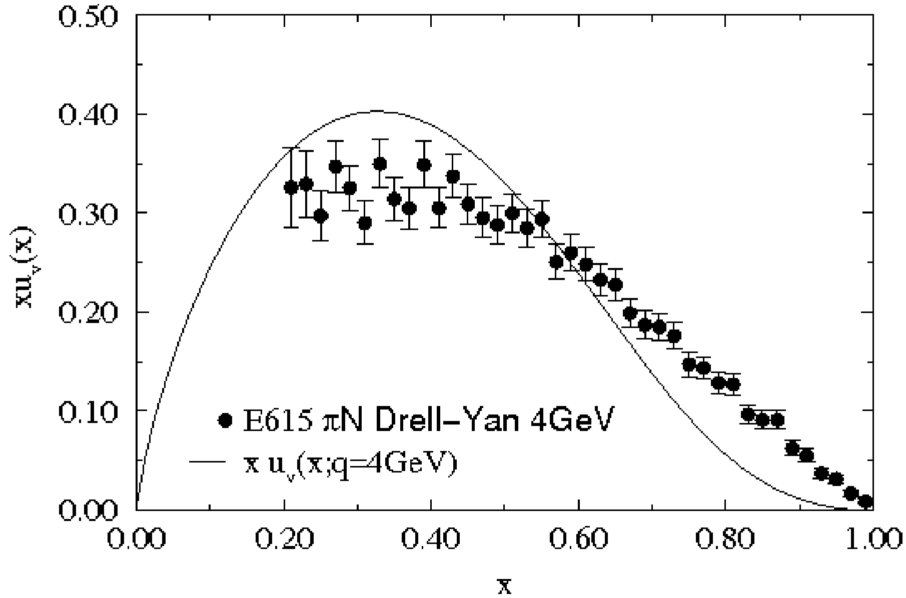

Figure 3: Existing data for the pion structure function from Drell-Yan Experiment E615 [23]. The solid curve is the calculation from Ref. [26].

measurement of pion structure functions exists. This makes it difficult to check the validity of the interpretation of the HERA data in terms of the meson-cloud model. The 12 GeV upgrade of JLab will allow access kinematics of $|t| < 0.2$ GeV^2, $Q^2 > 1$ GeV^2 and $M_x > 1.0$ GeV/c^2, which will enable us to probe the high and intermediate x region of the pion, where some data on the structure functions already exist from the pion-induced Drell-Yan experiments. A comparison of the x-dependence of the pion structure function deduced from the Sullivan process and the Drell-Yan process would provide a very stringent test of the pion-cloud model.

Other advantages of this measurement as here proposed for Jefferson Lab are: (1) The large angular and kinematic coverage for the recoiling proton (or recoil and spectator proton pair) detected using the proposed GEM-based detector, in coincidence with the scattered electron, will facilitate a detailed study of the Sullivan process as a function of several variables including the proton momenta and angles. (2) It is important to determine in one experiment the magnitude of the Sullivan process by detecting *both* the $p(e, e'p)X$ and $d(e, e'pp)X$, i.e. the $n(e, e'p)X$, reactions. The charged pion exchange process has the advantage of less background from Pomeron and Reggeon process [44] and the charged pion cloud is, moreover, double the neutral pion cloud in the proton. The measurements of the pion parton distribution in the Drell-Yan (Fermilab E615 and possibly at COMPASS in the future) is limited to charged pions. The proposed experiment will measure both the charged and neutral pion. This will facilitate a check of the validity of isospin symmetry and any other dynamical effects. Generally, the complementarity of the p $\rightarrow$ p and n $\rightarrow$ p reactions will assist in the identification of pion exchange and other contributions. Lastly, (3) The HERA measurements were obtained at small x and rather large Q^2. The Jefferson Lab kinematics, at larger x and smaller Q^2, will help study the

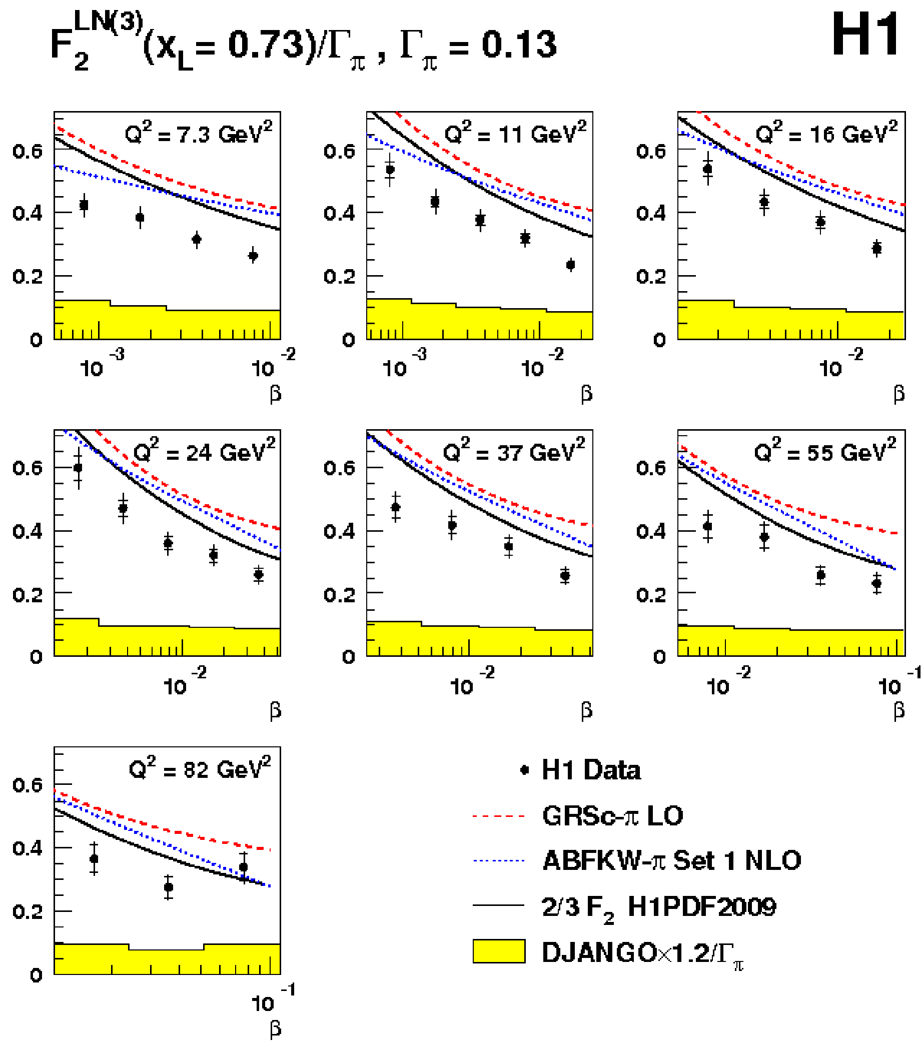

Figure 4: Pion structure functions measured by H1 [27] in comparison with parameterizations of various pion parton distribution functions. The Bjorken-x of the pion is denoted as β.

evolution of these effects between the two experiments.

The physics motivation for this experiment is, in summary, this: to pioneer a measurement of the Deep Inelastic Scattering (DIS) cross section, while tagging low-momentum recoil and spectator protons for the purpose of probing the elusive mesonic content of the nucleon structure function. The extraction of the mesonic structure of the nucleon from the tagged DIS cross section is inherently model dependent, and hence we will endeavor to examine all reasonable models that are currently available (such as Regge models of baryon production and Dyson-Schwinger equation (DSE) inspired models) or that may be available in the future. There is vibrant interest in this physics, as evidenced by recent workshops on the topic, for instance "Flavor Structure of the Nucleon Sea", held in July

2013 in Trento, Italy, "Exploring Hadron Structure with Tagged Structure Functions", held in January 2014 at Jefferson Lab, and "The Structure of the Pion", an invited session at the APS April Meeting held in 2015 in Baltimore, MD. Previous proposals to access this physics have been hindered largely by lack of low momentum reach, large backgrounds, or both [45]. It should be stressed that the measurement of the tagged DIS cross section is a worthy goal on its own right as there is scant existing data, particularly in the valance quark region, but the ultimate goal of the experiment is to extract information on the specific mesonic content of the nucleon from these tagged DIS cross sections.

To describe and further motivate the proposed measurement, we begin below with a description of tagged DIS kinematics and predictions from a phenomenological model for the mesonic component of the nucleon structure function (1.1). We then move on to a discussion of possible avenues for extraction of the pion structure function via the Sullivan process (1.2). Lastly, we discuss the broader impact of the experiment (1.3), and finally summarize the motivations in (1.4).

1.1 Tagged Deep Inelastic Scattering (TDIS)

In specific regions of kinematics, the observation of low-momentum recoil protons in the semi-inclusive reaction $eN \to eNX$ can reveal features associated with correlated $q\bar{q}$ pairs in the nucleon, sometimes referred to as the nucleon's "pion cloud", or more generally, the five-quark component of the nucleon wave function. In particular, at low values of the four-momentum transfer squared $t \equiv k^2 = (p - p')^2$, where p and p' are the initial and final nucleon four-momenta, the cross section displays, according to current models, behavior characteristic of pion pole dominance. Here, contributions from the exchange of non-pseudoscalar quantum numbers ($J^P = 0^-$), such as the vector ρ and ω mesons, are suppressed, and the pole-effect of these heavier mesons is less pronounced in our kinematic reach, leading to a qualitatively different t dependence than that arising from the pion pole. Furthermore, the contribution from the three-quark component of the wave function is highly suppressed because the momentum of the recoiling nucleon peaks at ~ 1 GeV/c.

1.1.1 Predictions of a Pion Cloud Model

Phenomenological models of the meson cloud [46, 47, 48] have been developed to study the contributions of the meson cloud to the structure function of the nucleon. The model [46] used in this proposal is described in some detail in Appendix A. Here we present the pion structure function and the tagged semi-inclusive structure function calculated using this model. The structure functions were studied as a function several kinematic variables, such as recoil proton momentum, t and x [46, 47, 48]. These studies form the basis for the projected experimental results, rates, and beam time request in this proposal.

According to the pion cloud model [3], the contribution to the inclusive F_2 structure function of the nucleon from scattering off a virtual pion emitted from the nucleon can be written as

$$F_2^{(\pi N)}(x) = \int_x^1 dz\, f_{\pi N}(z)\, F_{2\pi}\Big(\frac{x}{z}\Big), \tag{4}$$

where $z = k^+/p^+$ is the light-cone momentum fraction of the initial nucleon carried by the interacting pion. In the infinite momentum frame this coincides with the longitudinal momentum fraction.

While inclusive reactions require integration of the pion momentum over all possible values, detecting the recoil proton in the final state allows one to dissect the internal structure with significantly more detail and increase the sensitivity to the dynamics of the meson exchange reaction. The semi-inclusive structure function will be given by the unintegrated product

$$F_2^{(\pi N)}(x, z, k_\perp) = f_{\pi N}(z, k_\perp)\, F_{2\pi}\Big(\frac{x}{z}\Big), \tag{5}$$

where $k_\perp$ is the transverse momentum of the pion, and the unintegrated distribution function $f_{\pi N}(z, k_\perp)$ is defined by

$$f_{\pi N}(z) = \frac{1}{M^2}\int_0^\infty dk_\perp^2\, f_{\pi N}(z, k_\perp^2). \tag{6}$$

The dependence of the tagged structure functions on the kinematical variables that are measured experimentally can be studied by relating the magnitude of the 3-momentum

$\mathbf{k}$ of the exchanged pion in the target rest frame to the pion's transverse momentum $k_\perp$ and light-cone fraction z,

$$\mathbf{k}^2 = k_\perp^2 + \frac{\left[k_\perp^2 + (1 - [1-z]^2)M^2\right]^2}{4M^2(1-z)^2}. \tag{7}$$

Experimentally, the quantities most readily measured are the momentum of the produced proton, $\mathbf{p'}$, which in the rest frame is $\mathbf{p'} = -\mathbf{k}$, and the scattering angle $\theta_{p'} = \theta$ of the proton with respect to the virtual photon direction. In the limit $k_\perp^2 = 0$, the magnitude of $\mathbf{k}$ becomes

$$|\mathbf{k}|_{k_\perp^2=0} = \frac{zM}{2}\left(\frac{2-z}{1-z}\right), \tag{8}$$

which imposes the restriction $z \lesssim |\mathbf{k}|/M$. This relation is illustrated in Fig. 43 for values of z up to 0.2.

This is a critical guiding parameter for the proposed experiment. Since we seek to measure the low momentum region where pseudo scalar production dominates, the region of interest becomes $z \lesssim 0.2$. This corresponds to the measurable proton range, $60 \lesssim \mathbf{k} \lesssim 400$ MeV/c, of the radial time projection chamber discussed in detail below. It is important to note that, since $x < z$, this also determines both the x and Q^2 (given the maximum beam energy) of the experiment.

The predictions from the detailed study of the kinematic dependence of the pionic contribution to inclusive and semi-inclusive structure functions (described in Appendix A) are shown in Figs. 5 and 6. In Fig. 5 the x dependence of the inclusive structure function $F_{2p}(x)$ for the proton is compared to both the structure function for the full pionic content of the proton $F_2^{\pi p}(x)$ and the tagged, semi-inclusive structure function $F_2^{(\pi p)}(x, \Delta|\mathbf{k}|, \Delta\theta_{p'})$, for the indicated ranges in tagged, recoil proton momentum. The lowest momentum protons will be measured within the spectrometer acceptance, but clearly with lower statistics. Each momentum range corresponds by definition to a range in t, causing these low momentum protons to be of particular interest for extrapolation very close to the pion pole. It is planned that a range of t (proton momentum) points will be obtained at multiple values of x to map out this dependence. The full range of expected data are shown in a similar plot, along with an example of t extrapolation, in section 3 of this proposal.

Fig. 6 shows the equivalent neutron structure functions, but here compared to the strength of other physics channels: the tagged structure functions for $(\pi^- p)$, $(\rho^- p)$, and $(\pi^0\Delta^0 + \pi^-\Delta^+)$. The neutron target is planned to be tagged by two protons in coincidence with the scattered electron, one as was utilized successfully at backward angles in BONUS to identify the nearly free neutron in deuterium, and the other the recoil, tagged, semi-inclusive proton at more forward angles as discussed previously. The ρ component of this process is nearly negligible in comparison to the π, and the already small intermediate Δ resonance component to the process may be further reduced by a kinematic cut discussed in Appendix A, leveraging the differences in t_{min} as in Fig. 44. The momentum ranges as in Fig. 5 would appear nearly the same here for the neutron as they do for the proton and, conversely the other channels depicted here for the neutron would appear quite similarly for the proton. As with the proton, the full range of expected data are shown on a a similar plot in section 3 of this proposal.

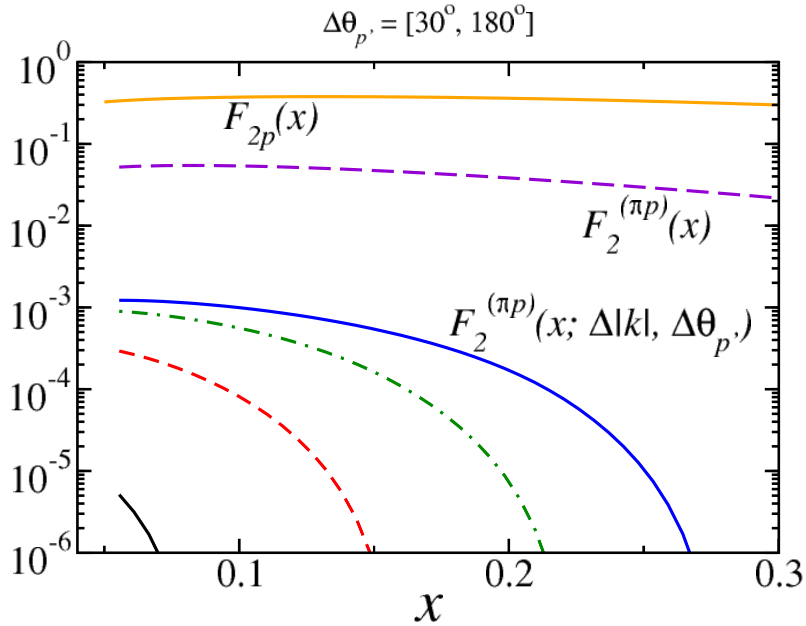

Figure 5: x dependence of the semi-inclusive structure function $F_2^{(\pi p)}(x, \Delta|\mathbf{k}|, \Delta\theta_{p'})$ (blue curve). For comparison, the total integrated πp contribution $F_2^{(\pi p)}$ to the inclusive proton structure function is shown (violet dashed), as is the total inclusive F_{2p} structure function (orange solid). The lower bands follow from varying the integration range $\Delta|\mathbf{k}|$; they correspond to $\Delta|\mathbf{k}| = [60, 100]$ MeV (black, solid), $\Delta|\mathbf{k}| = [100, 200]$ MeV (red, dashed), $\Delta|\mathbf{k}| = [200, 300]$ MeV (green, dot-dashed), and $\Delta|\mathbf{k}| = [300, 400]$ MeV (blue, solid).

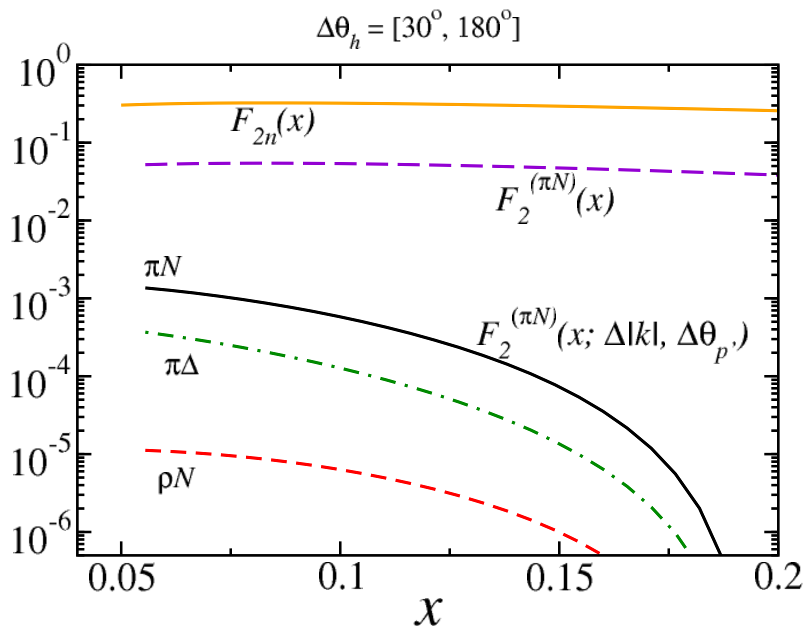

Figure 6: Structure functions as in Fig. 5, but now for the x dependence of $F_2^{(\pi p)}(x, \Delta|\mathbf{k}|, \Delta\theta_{p'})$ for charge-exchange in, e.g., the $n \to \pi^- p$ process. The tagged semi-inclusive structure function for $(\pi^- p)$ (black, solid), $(\rho^- p)$ (red, dashed), and $(\pi^0\Delta^0 + \pi^-\Delta^+)$ (green, dot-dashed) are compared with the inclusive structure function of the neutron $F_{2n}(x)$ (orange), and the fully-integrated $(\pi^- p)$ contribution $F_2^{\pi N}(x)$ (violet, dashed).

1.2 Extraction of the Pion Structure Function

In this experiment we will measure the semi-inclusive structure function of the recoil proton (neutron), denoted as the tagged structure function , F_2^T. The expected kinematic coverage in z and x is shown in Figs. 33 and 34, along with the yield for 10 days of beam for the measurement of the TDIS cross section. We will form the ratio R^T of the tagged (coincidence) to the DIS (singles) cross sections to measure the tagged structure function $F_2^T(x, Q^2, z, t)$. The measured ratio of cross sections may be written as:

$$R^T = \frac{d^4\sigma(ep \to e^{'}Xp^{'})}{dxdQ^2dzdt} / \frac{d^2\sigma(ep \to e^{'}X)}{dxdQ^2} \Delta z \Delta t \sim \frac{F_2^T(x, Q^2, z, t)}{F_2^p(x, Q^2)} \Delta z \Delta t. \tag{9}$$

Since the proton structure function $F_2^p(x, Q^2)$ is known extremely well over a wide range of x and Q^2, we can extract the tagged structure function $F_2^T(x, Q^2, z, t)$ as:

$$F_2^T(x, Q^2, z, t) = \frac{R^T}{\Delta z \Delta t} F_2^p(x, Q^2). \tag{10}$$

This ratio method reduces systematic uncertainties due to luminosity, electron trigger efficiency, and radiative corrections. We can, moreover, check many uncertainties by also measuring the cross section obtained from the DIS singles and comparing to the global $F_2^p(x, Q^2)$ inclusive data set. The pion structure function F_2^π can then be determined from the measured tagged structure function F_2^T as in Equations (5) and (6) in Section 1.1.

The pion flux $f_\pi(z, t)$ will be calculated using models of the mesonic content of the nucleon. All existing models will be examined for this purpose with the final choice determined by the model that best describe the data, with the ensuing model dependence addressed. Some of the current models that are available are:

i. The phenomenological model described in Sec. 1.1 and Appendix A.

ii. DSE inspired models. These have recently provided a prescription for a unified description of the pion's valence-quark distribution, its distribution amplitude, electromagnetic form factor and Generalized Parton Distribution function (GPD). This approach notably produces model independent quark distribution functions that are nearly independent of pion virtuality.

iii. Regge models of baryon and meson production.

1.3 Dyson-Schwinger Equation Inspired Models

In the modern language of QCD, the pion is simultaneously described as a bound state in quantum field theory and a Goldstone boson associated with dynamical chiral symmetry breaking (DCSB) [22]. This implies that an accurate description of the partonic content of the pion is essential for a clear understanding of QCD. The Dyson-Schwinger equations (DSEs) provide a non-perturbative approach to QCD by describing the pattern of chiral symmetry breaking and connecting them to experimental observables. One of the early predictions of QCD was that the large x pion valance-quark distribution should be given by $q^\pi(x) = (1 - x)^2$ [49, 28]. However, leading order analysis of pion Drell-Yan data seemed to suggest a $q^\pi(x) = (1 - x)$ [23] dependence. Recently, it has been shown that the impulse-approximation expression for the pion's dressed quark distributions that were used in these analyses ignore the contributions from the gluons which bind the quarks. When these gluonic contributions are accounted for in the framework of the Rainbow Ladder (RL) truncation of the Dyson-Schwinger Equation, the corrected valance-quark distributions are model independent and have well defined uncertainty [50]. The reanalysis of the Drell-Yan data using the new corrected expression for the dressed-quark distribution agrees well with the QCD prediction, as shown in Fig. 7. Using this RL truncation

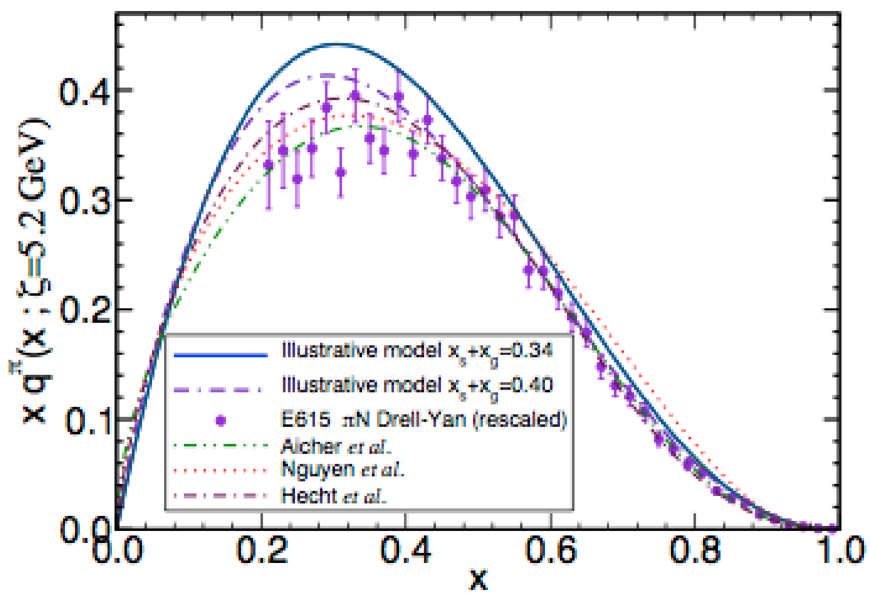

Figure 7: Several pion dressed-quark distributing functions and two illustrative models compared to the reanalyzed Drell-Yan data [50]

framework the authors have also outlined a procedure for the unification of the pion valence-quark distribution, its distribution amplitude and its elastic electromagnetic form factor. Recently, a procedure to obtain the pion's valence-quark GPD within the same framework has also been described [51]. In this new framework it has been shown that the form factor of a pion is essentially independent of its virtuality over a large range of pion virtualities (0 - 7 m_π^2), as shown in Figs. 8 and 9. Pion virtuality is defined as, $t_\pi = (P - P')$ where $P(P')$ are the initial(final) nucleon 4 vectors following a pion exchange.

It follows from this unified picture of the pion's valence-quark distribution that a virtuality-independent result for the pion form factor entails a virtuality-independent pion parton distribution function (PDF), based on Eqs. (5) & (6) in [51]. This is a powerful indication that it should be feasible to extract the pion structure function from the tagged DIS cross section measured at high pion virtualities, even substantially further from the pole than is here proposed.

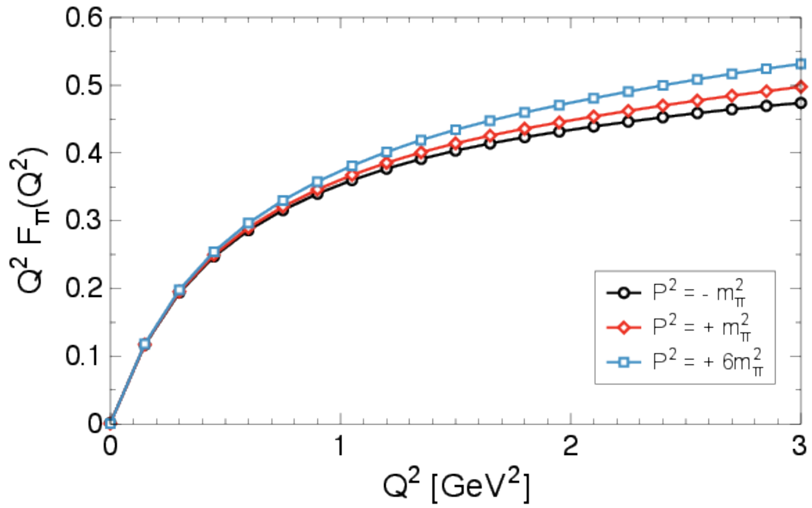

Figure 8: The pion electromagnetic form factor for pion virtuality ranging from 0 - $7m_\pi^2$ [52].

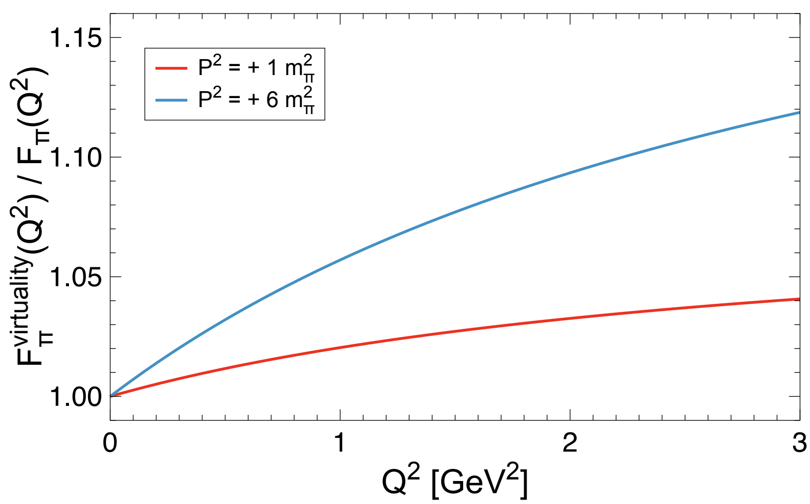

Figure 9: The ratio of off-shell to on-shell pion electromagnetic form factor for pion virtualities as indicated [52].

1.3.1 Corrections to the Extraction of Pion Structure Function

The extraction of the pion structure function will have to be corrected for a number of complications, such as non-pion pole contributions, Δ and other N^* resonances, absorptive effects, and the uncertainties of the pion flux. These corrections are minimized by measuring at the lowest recoil proton momenta possible. The low recoil proton momentum minimizes the absorptive correction since at lower momenta the pion cloud is further from the bare nucleon. The absorptive corrections are twice as large for the $n \to p$ reaction compared to the $p \to n$, but they are well known and have been recently calculated [53]. In addition, the low proton momentum ensures that the higher meson mass exchanges are suppressed by the energy denominator. The ratio of the pion contribution to sum of all exchange contributions for the phenomenological model (Sec. 1.1) is shown in Fig. 10, for both neutral and charged pions and for 3 different choices of the form factors used to suppress the wave function which controls the irregular behavior at large momenta (exponential, dipole and covarient dipole form factors). Here, the total includes ρ meson and Delta resonance contributions.

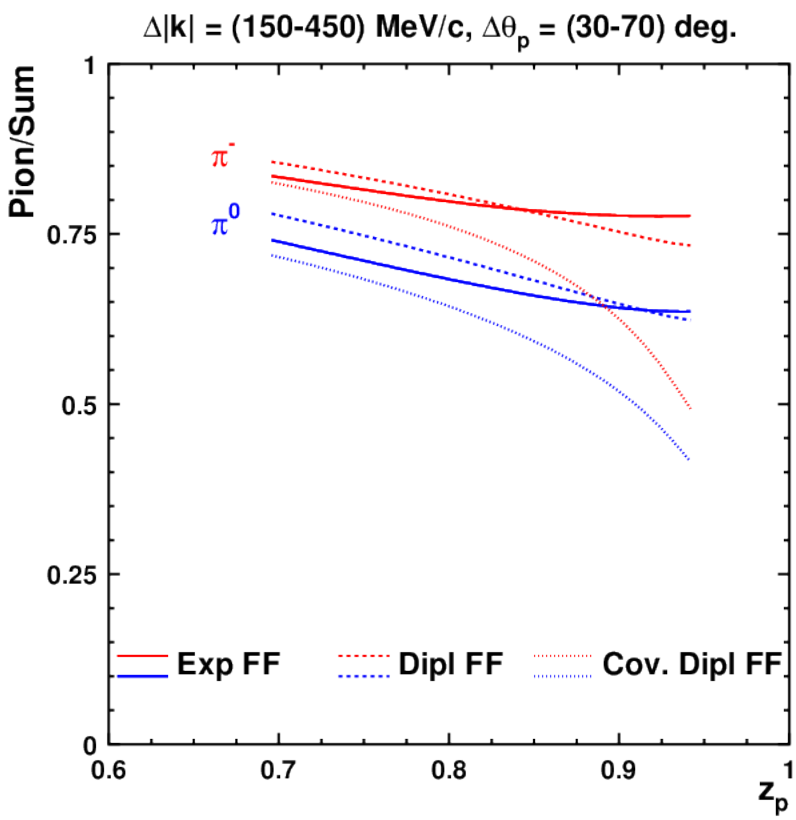

Figure 10: Ratio of pion to all contributions in the model of Ref. [46], for charged and neutral pions, shown for three different form factors used to control the irregular behavior at large momenta.

A somewhat analogous ratio plot is also shown in Fig. 11(left panel) for the charged pion case from Regge model work described in [54]. In this case, the sum total in the ratio denominator includes ρ meson and a Reggeon contributions, as are also shown in Fig. 11 (right panel). This approach has provided a good description of ZEUS and H1 data for leading neutron production in DIS [53], and has been calculated here by the authors for the kinematics of this proposed Jefferson Lab experiment. In Fig. 10 and 11, the definition of z_p corresponds to $1 - z$ used elsewhere in this proposal and so the measurements will be performed at the plotted range $z_p > 0.7$. The solid purple curve shows the pion fraction in the cross section. To get some feeling for the theoretical uncertainty, a maximal uncertainty assumption that the a_1 term was grossly overestimated was employed. Assuming that it is much smaller, the dashed-blue curve was obtained. The biggest uncertainty is here expected to be the a_1 term because: (1) It relies on diffractive $\pi + p \to p\rho + p$ data, which are available only at high energies; and (2) The $a_1 - N$ coupling was calculated purely theoretically, employing PCAC and the 2d Weinberg sum rule. The magnitude of this coupling has never been tested on data.

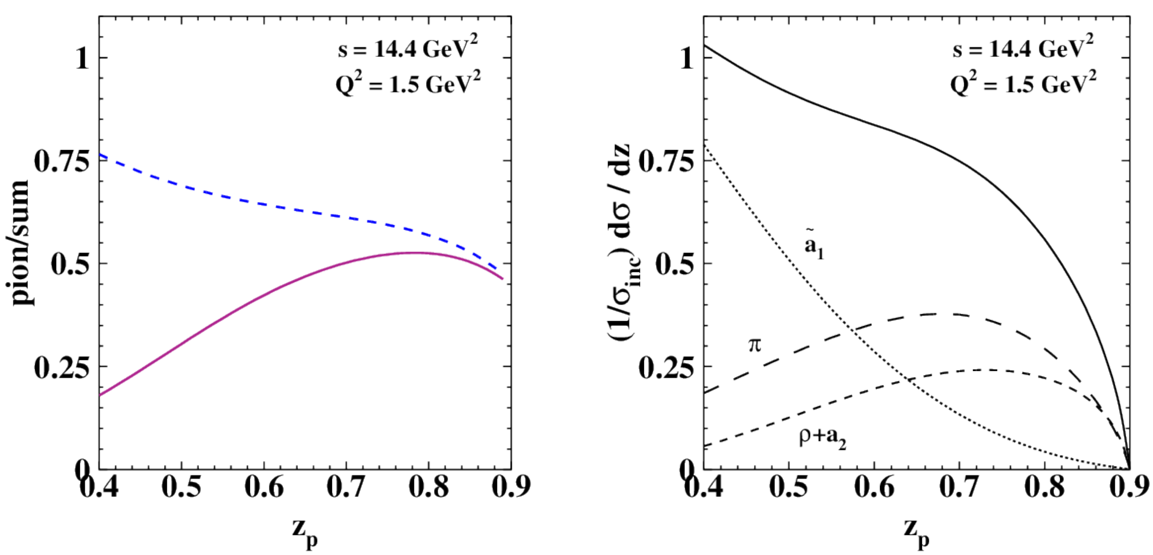

Figure 11: (left)Ratio of pion to all contributions in the Regge model of Ref. [53], for charged pions. The curves representing the range of theoretical uncertainty as described in the text.(right) Mesonic contributions to the nucleon in the Regge model of Ref. [53], for charged pions. Here and in the Figure above the z_p indicated is $1 - z$ used elsewhere in this proposal. The proposed measurements will be performed at the (here) plotted $z_p > 0.7$.

While the models agree that the pion is the dominant contribution to the meson cloud of the nucleon, the largest uncertainty in extracting the pion structure function arises from lack of knowledge of the exact pion flux in the pion cloud. This can be stated, alternatively, as the percentage of the measured structure function attributable to the pion. One of the main issues is whether to use the πNN form factor or a Reggeized form factor. The difference between these two methods can be as much as 20% [55]. From the N-N data the πNN coupling constant is known to 5% [56]. If we assume that all corrections can be performed with a 50% uncertainty and we assume a 20% uncertainty in the pion flux factor, the overall systematic uncertainty on our proposed measurement will be 24%.

However, by comparing to pionic Drell-Yan data at moderate x (where it is most reliable), we can have a measurement of the pion flux factor and its dependence on z and t. For example the pion structure function at $x = 0.5$ has been measured from the pionic Drell-Yan data to an accuracy of 5% [23]-[25]. The proposed data will have significant overlap with the Drell-Yan data, allowing us to leverage this precision and likely reduce our projected uncertainty. Moreover, we can normalize to this data at $x = 0.5$ to precisely study the critical question of the shape of the structure function at the higher x values.

1.3.2 Comparison of Neutron and Proton Data

This experiment will allow us to compare the tagged semi-inclusive cross-section and tagged structure functions of the proton and the neutron, for the first time in the valence regime. Moreover, all previous measurements of the pion structure function have been restricted to charged pions. This experiment will therefore be the first extraction of the structure function of the neutral pion. Beyond the basic isospin factor of 2, these measurements will provide kinematic reach to shed light on any dynamical effects that may exist. For example, comparison of the measurements by the H1 [27] and ZEUS collaborations by tagging forward-going neutrons or protons proved to be very informative. While neutron data proved to be dominated by π^+ exchange and could be used to extract the pion structure function at low x, the proton data had large contributions from the f_2 exchange in addition to π^0 exchange and was unusable for extraction of the pion structure function.

The measured cross sections from the proton and neutron in this experiment will be compared to a Regge model. In the Regge model, the contribution of a specific exchange i (pion, Pomeron, ρ, ω, a_2, f_2) is determined by the product of its flux $f_i(z,t)$ and its structure function F_2^i evaluated at (x_i, Q^2). Thus, for recoil (tagged) nucleon production at low p_T, we have;

$$F_2^T(x, Q^2, z) = \sum_i \left(\int_{t_0}^{t_{min}} f_i(z,t)dt \right) \cdot F_2^i(x_i, Q^2) \tag{11}$$

In the Regge model it is assumed that the neutral pion, the Pomeron and the f_2 will be the leading contributions to the cross section from a proton while the charged pion, ρ and a_2 are the leading contributions for the neutron [57, 54]. But, Regge phenomenology also predicts that the flux of Reggeons with isospin one (ρ and a_2) is only $\approx 3\%$ of the flux of Reggeons with isospin equal to zero (ω and f_2) [57]. It also predicts for the neutron that the contributions from charged pion exchange are an order of magnitude larger than the contributions from ρ and a_2 [58]. Pomeron exchange also does not give a significant contribution since diffractive dissociation is believed to be here only $\approx 6\%$ of the pion exchange contribution [58]. Moreover, the pion absorption corrections are twice as large for the neutron compared to the proton, but they are well known and have been calculated [53].

The measured tagged cross section and extracted tagged structure function will be compared to a Regge model where, assuming the dominance of a single Regge exchange, the differential cross section for recoil baryon production as a function of z at fixed t should be proportional to z^{-n}, where $n = 2\alpha(t) - 1$, and $\alpha(t)$ specifies the Regge trajectory of the dominant exchange. For pion exchange, n averaged over the t dependence is expected to be $n \approx -1$ while other Reggeons are expected to have $n > -1$. Thus, by comparing the z dependence of the cross-section from a proton and a neutron, we will be able to determine the dominant exchange mechanism. If the predictions for pion exchange are found to describe the data, the pion flux from the Regge model fits to hadron-hadron data will be used to extract the pion structure function. The comparison of data from hydrogen and deuteron (neutron) targets will serve as essential cross checks for the models used in the extraction of the pion structure function.

1.4 Impact for the Jefferson Lab 12 GeV Program and Beyond

The remarkably successful application of the quark-parton model in the description of deep-inelastic scattering (DIS) data over a very large kinematic domain has propelled this simple picture of the nucleon at high energies into becoming part of the common language employed by medium and high energy physicists. Massive and numerous global fitting efforts utilize perturbative QCD to extract the universal parton distribution functions from a host of high energy data including from decades of precision DIS experiments. Nevertheless, the QCD-improved parton model cannot, by itself, give a complete description of the structure of the nucleon at high energies. It is unable to (nor was it intended to) explain the spectrum of the nucleon's non-perturbative features. Here, effective degrees of freedom, for example in the form of a mesonic cloud of the nucleon, have been evoked to describe the long range structure of the nucleon. This has proved a reasonable approach in explaining for instance the deviation from the QCD-parton model prediction for the Gottfried sum rule and the flavor asymmetry in the sea quark distributions observed in Drell-Yan experiments. However, despite the various phenomenological successes of nucleon models which incorporate mesonic degrees of freedom, as yet there is scant experimental evidence unambiguously pointing to the existence of a mesonic cloud in high energy reactions. This experiment is designed to provide a clear signal of the presence of mesonic degrees of freedom in nucleon DIS, measuring where the pion contribution to the nucleon structure function should appear (i.e at relatively small Bjorken x ~ 0.1), while simultaneously measuring the well know DIS cross sections. Data from this experiment will, therefore, provide valuable input into high energy phenomenology and global fittting efforts for parton distribution functions by providing the size of the non-perturbative structure that needs to be addressed.

It is important to note also that this experiment may prove beneficial to a wide swath of the already-approved Jefferson Lab science program. There are multiple experiments planning to reach the factorization regime in semi-inclusive processes to access for instance transverse momentum dependent parton distribution functions as well as other semi-inclusive deep inelastic scattering physics such as flavor decomposition of the nucleon and single spin asymmetries. These experiments seek to measure at kinematics where the current fragmentation region may be cleanly separated from a target regime described as a nucleon via the well-known parton distribution functions. This latter aspect is not a valid approach if target fragmentation, is not also considered as a production mechanism that will impact the yield of measurable hadrons. Here, the mesonic component of the nucleon is likely for example to play an important role in final state interactions. Therefore, the proposed measurement may provide information valuable to precise interpretation of the underlying phenomena involved in a host of semi-inclusive scattering experiments in the Jefferson Lab 12 GeV era.

Moving into the future, the tagging approach pioneered here may pave the way for programs to map out the non-perturbative, mesonic, component of the nucleon both at Jefferson Lab in the 12 GeV era and at the proposed EIC, mEIC, and LHeC colliders. In the near term, this experimental approach could be leveraged further to tag semi-inclusive scattering such as $ep \rightarrow ep\pi X$, or to probe the strange quark content via $ep \rightarrow e\Lambda X$. At higher energies, the hard diffractive scattering measurements at HERA demonstrate the wealth of interesting physics specifically in the regime of these proposed new colliders. Because of the typically small cross sections, high luminosity as well as dedicated tagging detectors will be required; these are currently being included into electron-ion collider planning. Such measurements will also complement the new Drell-Yan data that will become available from experiments at COMPASS and Fermilab, and also possibly at the J-PARC facility. In all, this proposed Jefferson Lab experiment will provide a permanent, lower energy anchor for a wealth of future experiments.

1.5 Physics Motivation Summary

- This experiment will provide a first measurement of the tagged structure functions of the proton and the neutron in the valence regime.

- There is a great need for an experimental technique to probe the mesonic content of the nucleon. Few experiments have been able to directly probe the partonic components of the meson cloud of the nucleon, basically only scant data from hard diffractive processes at HERA and Drell-Yan to date. A range of models and theoretical work that predict the size and components of this cloud are available, but little data exists to constrain them.

- The well established quark flavor asymmetry in the nucleon sea can be explained in terms of the meson cloud model. The Sullivan process allows access to the meson cloud of the nucleon, and this direct measurement of this component will facilitate checks on the validity of this interpretation.

- Measuring the "recoil" proton at low momentum will facilitate reasonable extrapolation to the pion pole term, thereby facilitating a measurement of the pion structure function via the Sullivan process. The partonic structure of the pion, the lightest and simplest hadron, is not well measured over the entire Bjorken-x range and the predictions of models describing pion structure differ significantly.

- Measurements of the pion parton distribution in the Drell-Yan (Fermilab E615 and possibly at COMPASS in the future) are limited to charged pions. The proposed experiment will measure both the charged and neutral mesonic component. This will facilitate a check of the validity of isospin symmetry and any other dynamical effects. Generally, the complementarity of the p $\rightarrow$ p and n $\rightarrow$ p reactions will assist in the identification of pion exchange and other contributions.

- The nucleon structure function has been measured to multiple orders of magnitude precisely in x and Q^2. The standard description is given by valence quarks which radiate gluons, thereby generating sea quarks - all well described by DGLAP evolution. However, some part of the measured structure function data ($\approx 20\%$ in total) comes from scattering from non-perturbative, bound mesonic or meson-like objects in the nucleon. This experiment will provide a direct measure of a part of this effect, tagging the latter while simultaneously measuring the former.

- The measurement of tagged DIS at HERA explored diffractive scattering and extracted the pion parton distribution at small x and rather large Q^2 . At JLab, one can measure this at larger x and smaller Q^2 – advantageous kinematics for evolution between the two experiments.

- This is a potential gateway experiment to a broad program, in the near term at Jefferson Lab and in the far term at an electron-ion collider, to map out the non-perturbative, mesonic content of the nucleon.

2 Experiment

2.1 Overview

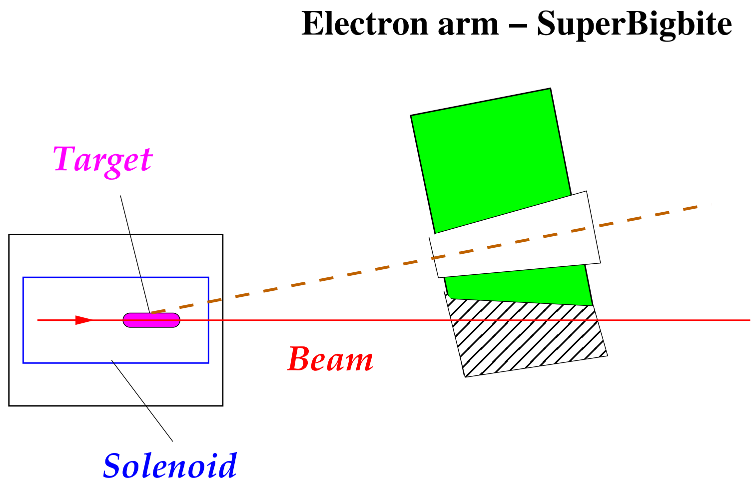

Figure 12: Schematic layout of the proposed experiment.

2.2 Experiment Luminosity

The subject of the proposed experiment is an essential feature of the nucleon internal structure, specifically, a quark-antiquark correlation related to the meson cloud associated with a (fluctuating/recoiling) nucleon. In spite of enormous developments in the field of nucleon structure over the last 65 plus years since the original Fermi and Marshall 20% number for the pion-nucleon component of the nucleon wave function, this estimate endures without significant change. However, the experimental signature of the pion in the nucleon remains under debate.

A fixed-target experiment at kinematics with modest momentum transfers and higher x will compliment the existing HERA measurements which investigated diffractive DIS in a collider regime with an 800 GeV proton beam on a 30 GeV positron beam. The proposed study of TDIS through detection of a very low energy proton "tag" in coincidence with a scattered electron DIS event will measure a very different part of the reaction space, one that may be rigorously evolved to the HERA kinematics, as well as related to the long-searched-for Sullivan process for accessing the pion structure function.

In this section we present a set of considerations concerning the Figure-of-Merit (FOM) for this experiment, a product of electron-nucleon luminosity ($\mathcal{L}$), electron detector acceptance (Ω_e), and recoil proton detection efficiency (η_p), required for TDIS investigation. The level of luminosity which may be used in the proposed experimental setup is constrained by the signal size and, critically, the experimental background rates.

The cross section of the inclusive DIS process for an 11 GeV electron beam scattered from a proton target is very well known, see e.g. the PDG report [59]. A traditional measurement of the DIS cross section with 1% precision and minimal DIS requirements on Q^2 and W^2 does not require much time with any electron spectrometer at Jefferson Lab, and experiments have been approved that will extend the existing body of such data in this kinematic regime from SLAC and other laboratories. The (unmeasured) percentage of such events coming from the meson cloud of the proton target should be approximately 20%. However, the fraction of DIS events in coincidence with a **low energy** proton is much smaller than the total meson-nucleon part of the wave function. According to recent calculations, described above, the fraction of DIS events with proton momenta below 400 MeV/c and at an angle within the detector acceptance (30 - 70 °), $F_{\pi p}(x_{_{Bj}}, \Delta k, \Delta\theta)$, is about 1% [60] (see Fig. 13).

Such a small fraction leads to a low rate of true coincidence events between the DIS-scattered electron and the recoiling, target proton. Therefore, the proposed experiment requires a large FOM and good control of accidental coincidences. The high rate of accidental coincidence events is the main problem for measurement of the TDIS cross section. These events are mainly due to a large rate of low energy protons produced in low momentum transfer reactions, such as small angle electron elastic scattering and meson photoproduction. In the deuterium target, one needs to also consider deuteron photodisintergration into low momentum proton-neutron pairs and the wider angular distribution of the protons involved in quasi-elastic electron scattering. There are four parameters which allow rejection of the accidental protons:

- The polar angle between the proton track and the beam direction.
- The correlation in time between an electron hit in the SBS and a proton hit in the RTPC.
- The correlation between the vertices of the electron and proton tracks.
- The correlation between the vertex of the spectator proton (tagging the neutron as a target, as in BONUS) and the recoil proton for the deuterium target.

2.2.1 Accidental Rates

Hydrogen Case There is a very high total rate of low momentum protons from low momentum transfer elastic electron-proton scattering. In the momentum range $k > 70$ MeV/c and luminosity $2.9{\times}10^{36}$ cm^{-2}/s, the rate is about ~170 MHz. However, these protons scatter predominantly in the angular range $78 - 88°$ (see Fig. 27 left panel). In comparison, the proton data of interest will be in a range only up to 65° maximum. The projected polar angle resolution of the RTPC of 1° will allow rejection of the range of angles where most of the elastically scattered protons are located. The background rate in the angular range to be used in the experiment, $30 < \theta_p < 70°$, is relatively small (0.2 MHz) as can be seen from Fig. 28.

The photoproduction mechanism leads to a higher rate in the angular range of interest, which was found to be $\sim$ 10 MHz from the hydrogen target at the proposed luminosity of $2.9{\times}10^{36}$ cm^{-2}/s in the momentum and angular range of interest. For additional information about this background, see the discussion of background simulations in Sec. 2.5, of this proposal.

The projected time resolution of the RTPC of 10 ns allows for a narrow 20 ns timing cut in offline data analysis. The length of the RTPC target cell (40 cm), combined with the good vertex resolution of the SBS spectrometer, will provide additional suppression of accidental events by a factor of 10.

The probability of protons to be accidentally detected in coincidence with the DIS electons can be calcualted as $P_{acc} = f_{prot} \times \tau \times (2.5\sigma_z/L)$, where f_{prot} is the singles proton rate ($\sim$ 10 MHz), τ is the timing cut/window (20 ns), σ_z is the vertex resolution (0.8 cm) and L is the length of the target (40 cm). The resulting total accidental probability is expected, then, to be **0.01** per electron. As shown in Fig. 13, the fraction of DIS events with protons within the detector acceptance with momentum $<$ 400 MeV/c is $\sim$1%, this implies a signal to accidental ratio of $\sim$**1**. However, we want to detect the lowest momentum protons that can be reasonably separated from the background. It is expected that we can extract the signal from the background for signal to accidental ratio of **1/10**, this implies that we can then measure proton rates as low as 0.1% of the DIS rate (shown by the magenta line in Fig. 13). This corresponds to protons with momentum as low as $\sim$200 MeV/c as can be seen from Fig. 13. The feasibility of extracting the signal from the background for signal to accidental ratio of 1/10 is discussed below and shown in Fig. 14.

Deuterium Case For the deuterium target at the same electron-nucleon luminosity of 2.9$\times 10^{36}$ cm^{-2}/s, there will be a large additional background rate coming from photo-disintegration protons. The estimated rate based on the photon flux is $\sim$ 90 MHz in the momentum range below 250 MeV/c. Moreover, there will be an even larger rate of the quasi-elastically produced protons, estimated to be $\sim$ 250 MHz. For detailed estimates see the discussion of background simulations in Sec. 2.5, of this proposal. This combined estimated rate of 340 MHz complicates investigation of TDIS from the neutron at low proton momenta. However, in the proton momentum range above 200 MeV/c the rate of protons drops dramatically. Therefore we calculate the accidental probability for several different bins of the forward (30$< \theta_p <$ 70) proton momentum. Moreover, the vertex resolution when detecting backward protons is about a factor of 2 better ($\sigma_{z2} \sim$ 0.4 cm). The rate for backward protons (100 $< \theta_p <$ 140 °) in the p_p = 70 - 200 MeV/c range is $\sim$ 200 MHz, which leads to a probability for accidental coincidence of **0.1** per electron.

For the triple coincidence between the electrons, forward protons and backward protons, the probability of the protons to be accidentally detected in coincidence with the DIS electons can be calcualted as $P^{(2)}_{acc} = f_{prot1} \times \tau_1 \times f_{prot2} \times \tau_2 \times (2.5\sigma_{z1}/L) \times (2.5\sigma_{z2}/L)$, where f_{prot1}, f_{prot2} are the singles proton rate for the forward and backward going protons, τ_1, τ_2 are the timing cut/window (20 ns), σ_{z1} and σ_{z2} are the forward and vertex proton vertex resolution (0.8 and 0.4 cm respectively) and L is the length of the target (40 cm). The resulting total accidental probability for different bins of the forward proton momentum is shown in Table. 1. These probabilities are in all ranges better than those for the Hydrogen target.

The projected level of the signal to accidental rate is illustrated in Fig. 14. The event distribution over $dz = z_p - z_e$ after other cuts are applied for a level of signal to background ratio of 1/10. The δz range represents the 40 cm target length, and it is important to note that the background events will be produced evenly along the target. In contrast, the data will be produced at a single vertex that we propose to measure with an accuracy

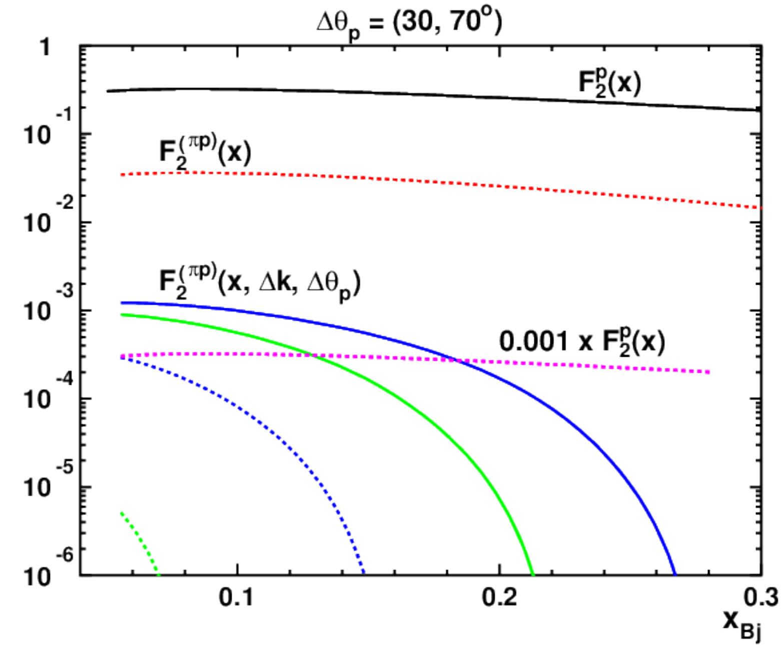

Figure 13: The proton SF F_2^p (black), the pion related part $F_2^{(\pi p)}$ (red dashed), and the fraction $F_2^{(\pi p)}(\Delta k, \Delta\Theta_h)$ vs x for the proton momentum intervals, Δk: in MeV/c - green dashed (60-100), blue dashed (100-200), green (200-300), blue (300-400) and the cut on the angle between the proton and the virtual photon momentum directions, Θ_p, between 30° and 70°. The dashed magenta line shows the level of signal for which signal to accidental ration is 1/10, demonstrating the range of proton momentum that can be reasonably separated from the backgrounds. It also shows the x range over which the mesonic contribution to DIS could be measured.

Forward proton momentum (MeV/c)	forward proton rate (MHz)	accidental coincidence probability
200-250	14	0.0015
250-300	7	0.008
300-350	4	0.0005
350-400	3	0.0003

Table 1: The total accidental probability for triple coincidence for backward ($100 < \theta_p < 140$ °) proton rate, in the $p_p = 70$ - 200 MeV/c range, of 200 MHz.

of 8 mm.

For verification of the analysis procedure and measurement at higher x up to 0.16 where the expected rate of e-p events is smaller (see Fig. 5), we plan to reduce the luminosity to $\lesssim 1 \times 10^{36}$ cm^{-2}/s and collect data for an additional period of 5 days. It is at these kinematics that the projected drop in the meson cloud distribution, and consequently in the fracture function, should be most apparent.

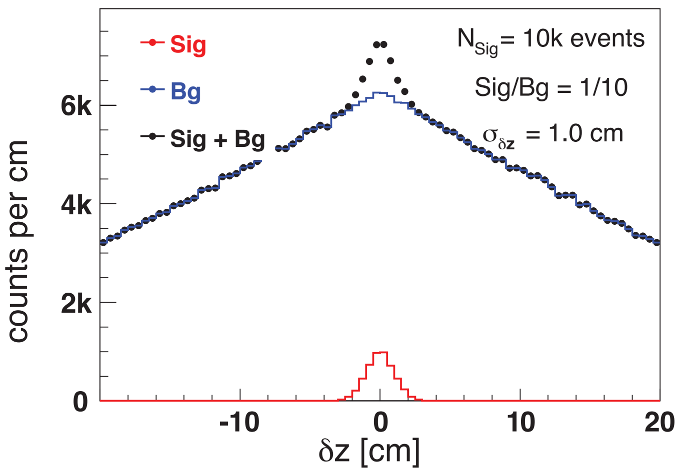

Figure 14: The projected event distribution over $\delta z = z_p - z_e$ for a ratio of signal to background of 1/10 (in the "2-σ" area).

2.3 Recoil Detector

Detection of a soft nucleon is complicated by a large intensity of the secondary electrons, photons, and soft nucleons produced in the interaction of the high energy electron beam with the target. A proton detection option as employed by the BONUS and CLAS eg6 experiments has several essential advantages over neutron detection:

- The ionization density in the soft proton track for the momentum range 60-400 MeV/c is very high, which allows effective suppression of the secondary electron and soft photon induced signals.

- The protons of interest (2.0 - over 30 MeV kinetic energy) have a momentum component perpendicular to the beam direction much larger than the typical perpendicular momentum of the secondary electrons, which allows use of magnetic separation of the proton and electron background using a solenoidal magnet.

- The proton track allows for reconstruction of the event vertex and direction, which are powerful means for rejection of accidental events.

- The proton detector readout segmentation could be on the level of 10^5 or above, which is at least a factor of 100 times higher than practical for a neutron detector.

The recoil detector will be fundamentally the same as the cylindrical RTPC being developed for the experiment to measure the structure function of the free neutron (E12-06-103, or BONUS-12), the latter being based on the very successful cylindrical RTPCs that were employed for the BONUS and CLAS eg6 experiments as pictured in Fig. 15. The proposed RTPC will, however, utilize a different solenoid. This is an existing solenoid, shown in Fig. 16, with a 400-mm warm bore, a total length of 152.7 cm, and a superconducting coil that operates with a 47 kG magnetic field in the center of the magnet. This solenoid belongs to the UVa collaborators on this proposal, and is currently being used for tests of LHC detector electronics. Any stray field of the solenoid on the asymmetric iron of the SBS, could be symmetrically balanced with an iron yoke. While this approach certainly needs a full analysis for exact design, we note that this is reasonably standard, and that a solenoidal field surrounded by an iron yoke is typical for collider geometry. The heating of the superconducting coil is not expected to be an issue for this proposal because of the relatively small luminosity and the coil being immersed in liquid He.

Simulation studies have shown that increasing the radial drift region by a factor of 2 compared to the BONUS and eg6 RTPC detectors can provide at least a 50% relative improvement in the momentum resolution, as well as extending the momentum range of the detector. The larger bore of this magnet will facilitate the RTPC having a larger radial drift distance than that proposed for BONUS-12. The enhanced drift region will facilitate measurements of proton momenta up to 400 MeV/c with a resolution of 3%. The length of this magnet is also a help, allowing us to use a longer (40 cm) target for improved background rejection and luminosity.

The proposed TDIS RTPC will be 40 cm long and consist of an annulus with inner radius of 5 cm and an outer radius of 15 cm. The amplification of the drifting electrons will be achieved by three layers of cylindrical Gas Electron Multiplier (GEM, see Ref. [61])

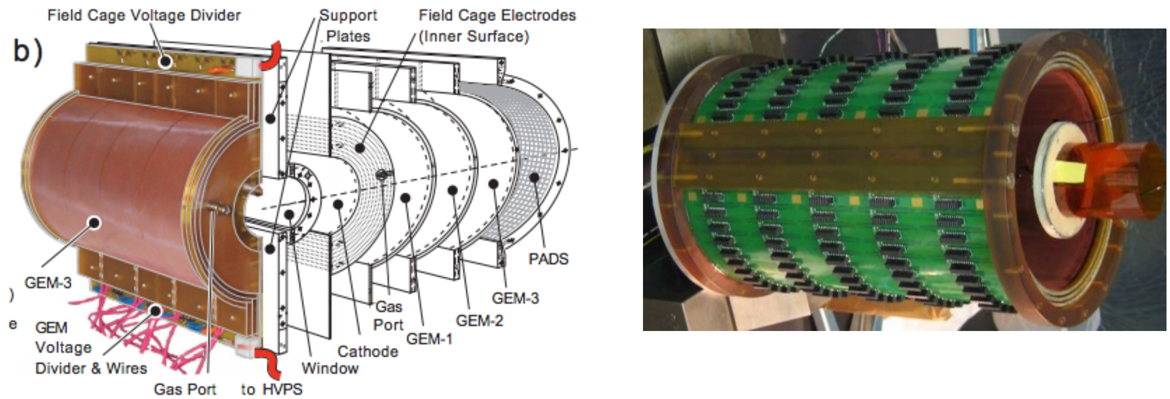

Figure 15: (left) Photograph of the BoNuS RTPC, showing the left module with the readout padboard removed and a complementary exploded view exposing the components of the right module. (right) Photograph of the eg6 RTPC during assembly.

foils at radii of 15 cm. This will be surrounded by a cylindrical readout surface featuring elongated pads. GEMs are 50 μm thick polyamide foils coated on both sides with a 5 μm copper layer and punctured with 70 μm holes. The distance between these holes is about 140 μm. By applying a voltage in the range of 200 V to 300 V across the two copper layers a very high electric yield is formed inside the holes. Ionized electrons from the maximally ionizing low momentum protons drifting towards the GEM foil produce an avalanche of secondary electrons when captured and accelerated through the holes. The total gain in GEM will be of the order of 10^3, which is far below the limit of gain achievable with GEM-based detectors. The electrons are transferred to the next GEM foil and, after passing three GEM foils, the resulting electron pulse will be detected on the readout plane. The full length of the RPTC could be be closer to 60 cm to accommodate protons emitted at angle as small as 30° relative to the beam direction.

As with BONUS and CLAS eg6, materials between the target and the sensitive detector volume have to be minimized to prevent energy loss of the protons and to minimize the interaction of background particles which reduce efficiency of magnetic confinement of the low energy background. The tracking region will be formed by a set of light weight straws, a set of wires, and the GEM. The straws will hold a 2 μm gold plated kapton film cylinder. The wires will be used to increase the electrical field at a larger radius. To further minimize background events, a thin wall Be tube will be used for the first 50 cm of the beam line downstream from the target. After that a larger, standard Al pipe will provide connection to the exit beam line through the SBS magnet to the beam dump. The window between the low pressure, cold RTPC and atmosphere will be made from a pre-deformed 0.5 mm aluminum plate with a supporting grid of steel bars. The recent design of a cylindrical GEM chamber at INFN Frascati for the KLOE experiment [62] will be explored for potential improvements.

The RTPC will be filled with a He based mixture which allows reduction of the secondary background in the chamber due to low energy photon induced signals. A study of GEM operation with low pressure He-based mixtures has been demonstrated in the reference [63]. For this proposal we assumes an average electric field of E =500 V/cm,

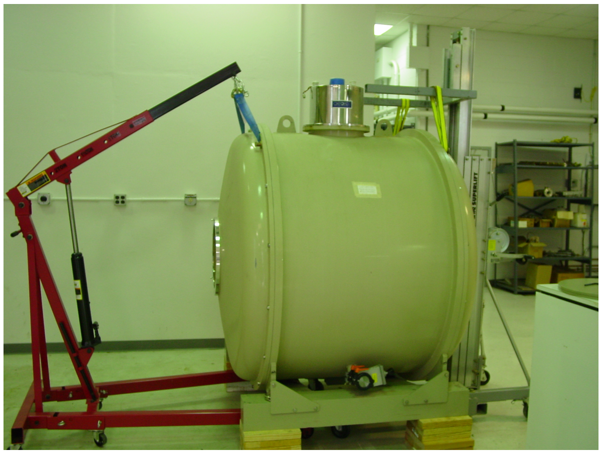

Figure 16: Photograph of the available 5T solenoid.

an average magnetic field of B= 4.7 T, and a temperature of T= 77 K. The operating pressure for the RTPC would be approximately p = 0.2 atm. Since the drift gas properties go as E/p, this situation is equivalent to the case of 2500 V/cm at 1 atm. The drift gas assumed here is 90% He and 10% CH4 as the quencher. The vapor pressure of CH4 at 77 K is sufficient to get this concentration in the mixture. The information given here is based on the extensive simulations done and data compiled by Sauli and Sharma and by Sharma and Assran [64]. The mixture could also be further optimized as needed. If it turns out that more stability is needed, it could be achieved by increasing the amount of CH4 in the gas mixture, for example, by increasing the operating temperature of the RTPC. Increased temperature increases the vapor pressure of CH4, resulting in a higher amount of CH4 in the mixture.

The drift velocity for above operating conditions is approximately 2 cm/s. At the 500 V/cm electric field, the drift velocity is at a relative plateau region, where it changes by only about 10% for a 25% change in either the electric field or the pressure. Given the drift distance of 10 cm in the RTPC, the drift time range would be approximately $5\mu s$. The Lorentz angles for He based gas mixtures is about a factor of 3 smaller than the corresponding Lorentz angles for Ar based mixtures. For the proposed E and B fields, the Lorentz angle would be around 35-degrees for the proposed gas mixture.

The longitudinal diffusion is approximately 350 $\mu m/cm^2$. For the ∼10 cm drift from the furthest cluster the maximum longitudinal diffusion is expected to be $\sim 1mm$ (with a time spread of 50 ns); however, the relevant quantity for background suppression is the signal time with respect to the trigger, which is determined by the cluster closest to the readout, with a drift distance of about 1 cm. For these cluster the dispersion would be approximately 350 μm, with a time spread of approximately 15 ns. This is sufficient to achieve the desired 10 ns time resolution. The transverse diffusion is approximately 225 $\mu m/cm^2$. For the 10 cm drift from the furthest cluster, the maximum transverse diffusion would be approximately 750 μm; which is less than the readout pitch of 1 mm and has no significant effect on the position resolution.

The readout will be in a pad configuration with each pad having dimensions of 1 mm (azimuthal) x 21.25 mm (z). The readout is a 2D u-v strip readout with a strip pitch of 1 mm in either direction. With this strip pitch we assume a 300 μm position resolution from the RTPC. Given this high resolution from the RTPC, the limiting factor for the vertex reconstruction is the electron vertex from the SBS. The overall vertex resolution is assumed to be 8 mm. In order to reduce the per channel occupancy, each strip in both u and v layers is separated into 21 mm segments. Each strip segment is individually bridged by a via to a 50μm wide connection strip on the back of the readout plane. This connection strip connects the strip segment to its own readout channel. The connection strips for u strips and for v strips will be on two different layers insulated from each other on the back of the readout plane. The outermost cylindrical layer of the detector will be the readout board made out of a flexible circuit board, with traces that will connect to front end electronic cards located at the end(s) of the cylindrical detector. Improvements in GEM electronics over the last few years will allow for the readout cards to be placed at the end(s) of the RTPC cylinder. This will allow some further increase in the drift region as compared to the BONUS and eg6 experiments by removing the need for radial on-board amplification.

To read out signals from the detector, we will use the APV25 chip based Scalable Readout System (SRS) developed at CERN by the RD51 collaboration. The APV25 chip is an analog chip developed by the Imperial College London for the CMS experiment silicon trackers. It has been subsequently adopted by several experiments, such as the COMPASS trackers at CERN, STAR FGT at BNL and others. It is also planned for the tracking detectors in the SBS project. The APV25 chip samples 128 channels in parallel at 20 MHz or 40 MHz and stores 192 analog samples, each covering 50 ns or 25 ns, per channel. Following a trigger, up to 30 consecutive samples from the buffer are read-out and transmitted to an ADC unit that de-multiplexes the data from the 128 channels and digitizes the analog information. Operating in the 20 MHz mode with the 30 sample readout will give a dynamic time range of 1.5 μs for the APV readout. This is sufficient to cover the drift time range of the TPC, which is expected to be approximately 1 μs corresponding to the increased drift velocity in the He-based gas mixture. Note that the readout electronics are are located outside the cold (77K) region of the detector.

The selection of the chip for the readout system will be changed if the drift time exceeds the capabilities of the APV25. The 25 ns APV readout has been shown to provide timing resolution better than 8 ns [65]. Given the expected 5μs time range required for this experiment, the APV chip may not be optimal for this experiment. On the other hand, the DREAM chip, recently developed by the Saclay group, offers the time range we need and gives the flexibility to optimize parameters as needed for this experiment. A time resolution as low as 4 ns was recently demonstrated [66] in the LHCb GEM chamber with a similar readout where the GEM signal was first integrated and then digitized. For this proposal we have assumed 10 ns timing resolution, and we continue to follow new improvements being made to both the APV25 and DREAM chips.

The SRS system consists of the following components:

- APV-25 hybrid cards mounted on the detector. These cards contain the 128 channel APV-25 chip which reads data from the detector, multiplexes the data, and transmits analog to the ADC card.

- SRS ADC unit that houses the ADC chips that de-multiplex data and convert into digital format.

- SRS FEC card which handles the clock and trigger synchronization. A single FEC and ADC card combination has the capability to read data from up to 16 APV hybrid cards.

- Scalable Readout Unit (SRU), an optional component not shown in the figure, which distributes the clock and trigger synchronization to the FEC cards. One SRU handles communication between multiple (up to 40) FEC cards and the data acquisition computer.

- The data acquisition computer, which could be part of a larger DAQ system as one of the readout controllers.

Work is currently underway to incorporate the SRS system into the CODA data acquisition framework at JLab. Our plan is to be as compatible to the existing SBS GEM tracker module readout as possible.

2.3.1 Target cell

The proposed TDIS target inside the RTPC is significantly different from those previously utilized. The target vessel is here a cylinder with an inner radius of 5 mm and 40 cm long. It can be considered as a self-supporting balloon. The target will be gaseous Hydrogen or Deuterium at 77 $^{\circ}K$ and 1 atm. In order to minimize the energy loss of the protons of interest, we have reduced the material of the target wall as much as possible, down to 10 micrometers of aluminum. The larger diameter of the cell and the aluminum walls are necessary given the high luminosity of the proposed experiment. The lower temperature of the target (liquid nitrogen) and increased length of the cell allow reduction of the gas pressure in the target (from 7 atm used in BONUS) to 1 atm.

The resulting threshold and energy loss for low energy protons are presented in Tab. 2, as calculated by our Geant4 Monte Carlo model of the RTPC. This is a modification of the Monte Carlo successfully utilized to analyze the BONUS experiment.

p(MeV/c)	50	75	100	150	225	325
E_{kin}(MeV)	1.33	3.00	5.31	11.9	26.6	54.7
90 deg						
at TargetWall	1.24	2.95	5.28	11.9	26.6	54.7
after TargetWall	0.75	2.71	5.13	11.8	26.6	54.7
after Cathode		2.43	4.97	11.7	26.5	54.6
at 1st GEM			4.47	11.6	26.4	54.6
45 deg						
at TargetWall	1.21	2.93	5.27	11.9	26.6	54.7
after TargetWall	0.45	2.59	5.06	11.8	26.5	54.6
after Cathode		2.11	4.82	11.7	26.5	54.6
at 1st GEM				11.4	26.4	54.6

Table 2: Monte Carlo results for kinetic energy loss of protons starting at the indicated momenta on top line, presented for various positions as the protons encounter structures while radially traversing the RTPC.

The actual energy loss through the target gas and walls, as well as through the various materials in Tab. 2, depends on the proton track angle when encountering the material. Fig. 17 depicts Monte Carlo results for protons escaping the target, demonstrating this angular dependence for initial proton angles as well as the minimum momentum threshold ($\gtrsim$ 56 MeV/c) for the experiment. These threshold particles just barely penetrate the cathode.

2.3.2 RTPC Calibration

The proposed measurement of the tagged DIS cross section will require good knowledge of the various detector acceptances and efficiencies. The fully inclusive electron-proton and electron-deuteron cross sections are well known from experiments in this kinematic regime at Jefferson Lab and SLAC [67]. Comparing our untagged DIS measurements with these

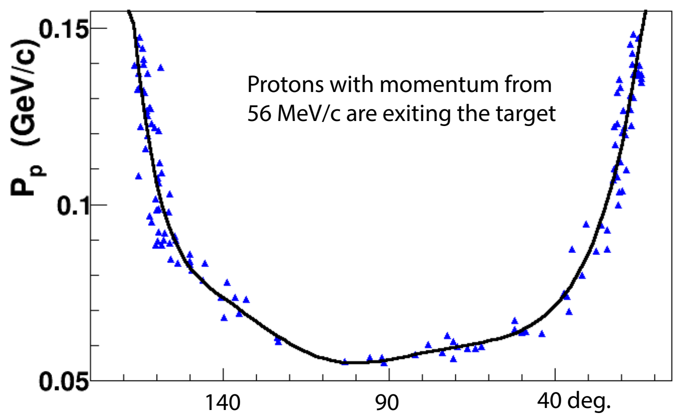

Figure 17: Minimum proton momentum as a function of angle for protons exiting the RTPC target.

data will allow for precision checks of the acceptance, efficiency, and other corrections used for the SBS electron spectrometer analysis.

The RTPC will also require study and calibration. The BONUS experiment was not able to make precise acceptance and efficiency corrections to the RPTC data to measure the neutron cross section directly using the tagging technique, but rather had to simulate as well as normalize to a model F_2^n/F_2^d ratio for an assumed-known kinematics within the data set. This contributed significantly to the uncertainty of the measurement [68]. We could perhaps employ a similar approach, but suggest also that different quantities may be used as well to extract the RTPC acceptance and efficiency.

Some initial calibration can be done by using the copious proton tracks from elastic electron-proton scattering. At production luminosity there will be several accidental elastic proton tracks distributed evenly along the target for in every $e-p$ DIS event. These protons are well separated from the protons of interest because, to be at the same momentum but generated by elastic events, they are necessarily kinematically directed almost perpendicular to the beam.

It will be particularly productive to use quasi-elastic electron scattering from the deuteron for the RTPC calibration. The energy and direction of the spectator proton may be determined in a quasi-elastic reaction using a scattered electron in the SBS in combination with a neutron measured with the (relocated) SBS Hadron Calorimeter (HCAL). The move-able HCAL detector would not be a part of the SBS for this experiment, and could be placed beam right at optimum kinematics to record neutrons for this calibration measurement. In such a way we can predict the distribution of protons of energy, for instance 5-27 MeV (100-225 MeV/c), in the directions required for the RTPC calibration. A comparison between the measured proton spectra and the proton distributions expected in the RTPC from quasi-elastic neutrons in HCAL will provide a check on the RTPC proton acceptance and efficiency corrections. If the suggested quasi-elastic HCAL neutron measurement is for some reason not available to the proposed measurement, it will be possible though not optimal to work through simulation and geometry as was done for the CLAS6 experiments.

The proposed calibration will be performed at an electron-nucleon luminosity of 0.3×10^{36} Hz/cm^2 with an electron beam energy 4.4 GeV and SBS angle at the same angle of 12 degrees as during the production TDIS run. The projected rate of electron-neutron quasi-elastic events in SBS is around 1000 Hz. The average neutron momentum will be 970 MeV/c. Using HCAL located at a distance of 15 meters (60 degrees relative to the beam direction) we estimated that the coincidence $e-n$ rate will be approximately 70-80 Hz. Neutron momentum will be within a cone with an average angle relatively the beam of 60° an opening of ±4°. At such a low luminosity the spectator protons will be

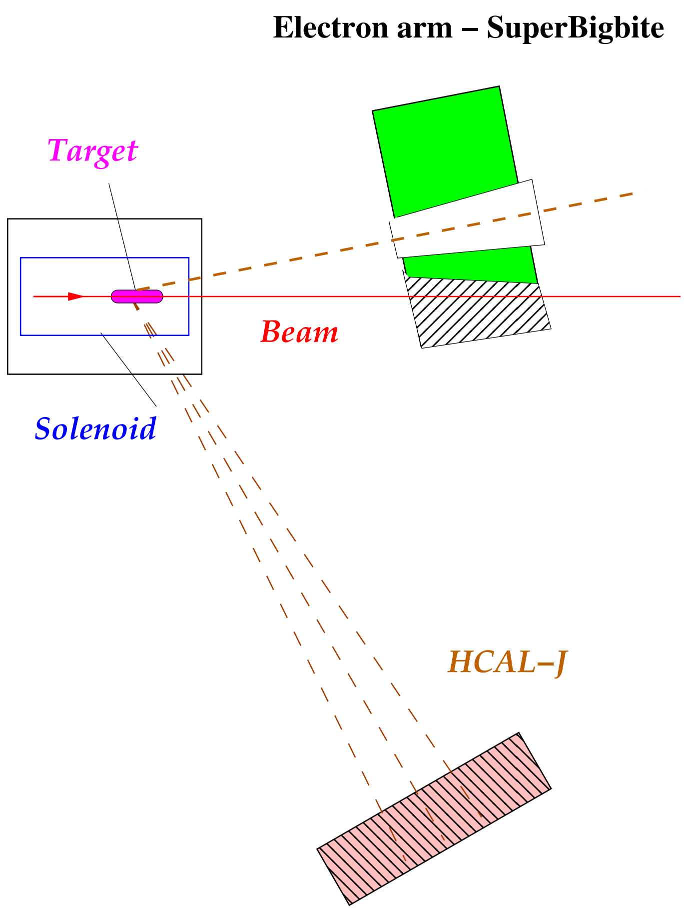

Figure 18: Setup for RTPC calibration

easy to identify and use for RTPC calibration. One day of such a measurement provides more than 6 million tagged proton events which would allow detailed study of RTPC.

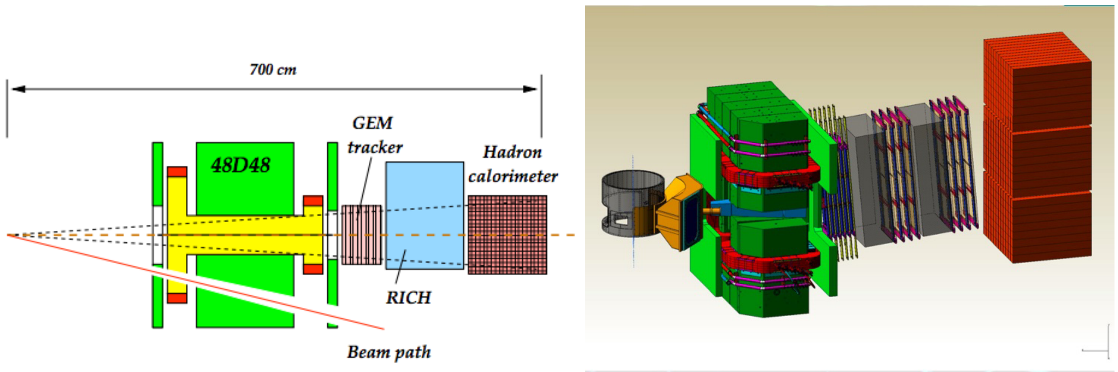

Figure 19: A schematic (left) and a CAD drawing (right) of the Super Bigbite Spectrometer

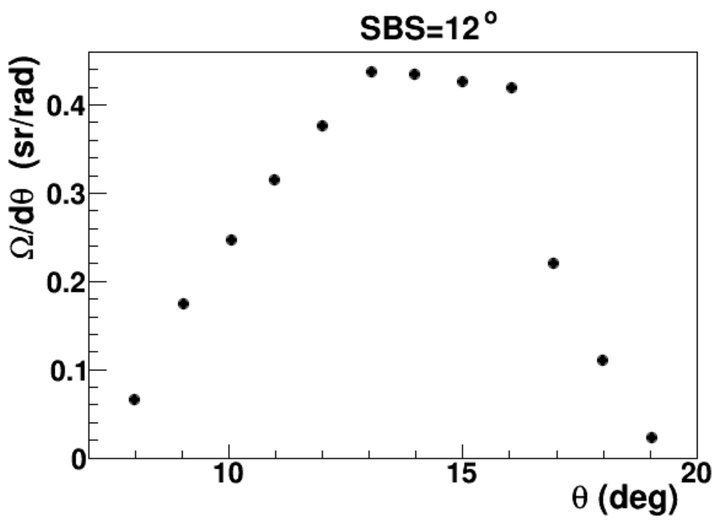

Figure 20: Solid angle vs. polar angle at the 12° SBS position.

2.4 The Super Bigbite Spectrometer

The Super Bigbite Spectrometer (SBS), currently under construction and fully funded by DOE NP, consists of a dipole and a modular detector package. An important feature of the SBS is a beam path through the opening in the right side yoke of the magnet, which allows it to be placed at forward angles as small as 3.5°. For the proposed experiment the SBS magnet (front face of the yoke) will be placed 2.0 m from the target allowing for a 50 msr solid angle around a 12° central angle. The large out-of-plane angle of SBS provides significant coverage in azimuthal angle (about 20% of 2π). Figure 20 shows the spectrometer solid angle vs. scattering angle for such a setting. In the proposed experiment we plan to use the large GEM-based chambers currently under construction for the SBS G_E^p experiment polarimeter as the main tracking planes. We plan to use five out of ten constructed planes and concentrate the readout electronics of all ten planes in those five. These chambers will each cover a 60 cm x 200 cm area, and the concentrated electronics will then allow reading of every readout strip. These chambers were tested in such a configuration and a spatial resolution of 60-70 μm was obtained.

The combination of an electromagnetic calorimeter (the CLAS-6 Large Angle Calorimeter or LAC) and threshold gas Cherenkov counter (the HERMES RICH or GC-SBS) will be used for trigger and particle identification purposes. The LAC is discussed in some detail below. The Gas Cherenkov will be a straightforward modification of the existing ring imaging Cherenkov (RICH) detector planned to be utilized in the approved SBS experiment E12-09-018 - basically filling the tank with CO_2. The combination of these two detectors will be sufficient for the electron particle identification purposes of this experiment.

2.4.1 CLAS6 Large Acceptance Calorimeter

The SBS was originally designed to be a hadron spectrometer. In order to use SBS as an electron spectrometer with good pion rejection capability we will replace the hadron calorimeter with the safely salvaged Large Acceptance Calorimeter (LAC) from the CLAS6 detector.

The conceptual drawing of the internal structure of the LAC is shown in Fig. 21. The LAC module has a rectangular shape with a sensitive area of 217 x 400 cm^2 and consists of 33 layers, each composed of a 0.20 cm thick lead foil and 1.5 cm thick NE110A plastic scintillator bars. The total thickness is about 12.9 radiation lengths or 1 hadronic absorption length. Each scintillator layer is protected from contact with the lead by 0.02 cm thick Teflon foils. The width of the scintillators is roughly 10 cm and increases slightly from the inner layers toward the outer layers to provide a focusing geometry. Scintillators in consecutive layers are rotated by 90 degrees to form a 40 x 24 matrix of cells with area approximately 10 x 10 cm^2. The module is vertically divided into two groups: an inner (first 17 layers) and an outer (16 layers) groups. Each group has its own light readouts. Scintillators lying one on top of the other with the same orientation form a stack. For each stack the light is collected at both ends separately using light guides coupled to EMI 9954A photomultiplier tubes. For each module there are 128 stacks and 256 photomultipliers [70].

The LAC energy resolution for electromagnetic showers is 7.5 $\pm$ 0.2 % [70]. Combined with CLAS, the pion contamination is less than 1% for cuts that give a detection efficiency of 95% for 2 GeV electrons.

A Geant4 simulation has been performed to study the LAC for this proposal. Fig. [22] shows the LAC in this Geant4 program. Our results indicate that grouping the first 17 layers into the inner part should provide a good choice and that the particle identification be cut should include two parts: $E_{tot}/P > 0.33$ and E_{in} cuts. Here, E_{tot}/P is the fraction of energy deposited in the LAC compared to the total momentum of the particle, and E_{in} is the energy deposited in the inner layers only. The optimum cut value for E_{in} is momentum dependent. The results indicate that the pion rejection fractions will be 89%, 92%, 95% and 96.5% for particles with momenta 1.0, 2.0, 5.0 and 8.0 GeV/c, respectively.

The pion to electron rate in the SBS is shown in Fig. 23, for the proposed hydrogen target. In the scattered energy range below 3 GeV the combined (RICH and LAC) pion rejection will be above 10,000, which will reduce the pion contamination to below 1%. For energies above 3 GeV the rejection from the gas Cherenkov will be reduced.

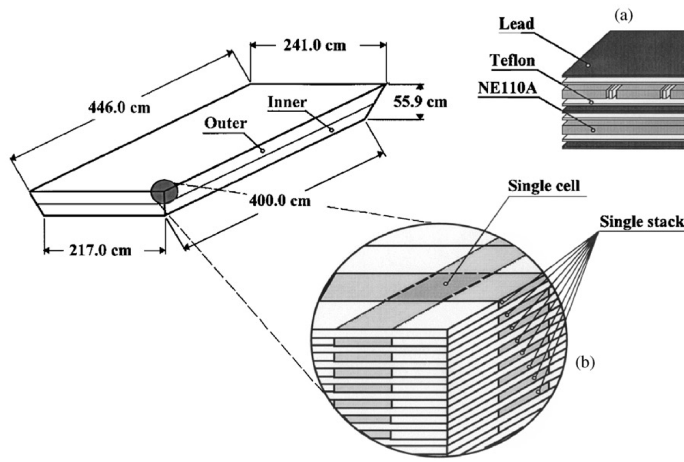

Figure 21: The conceptual drawing of the internal structure of the LAC module.

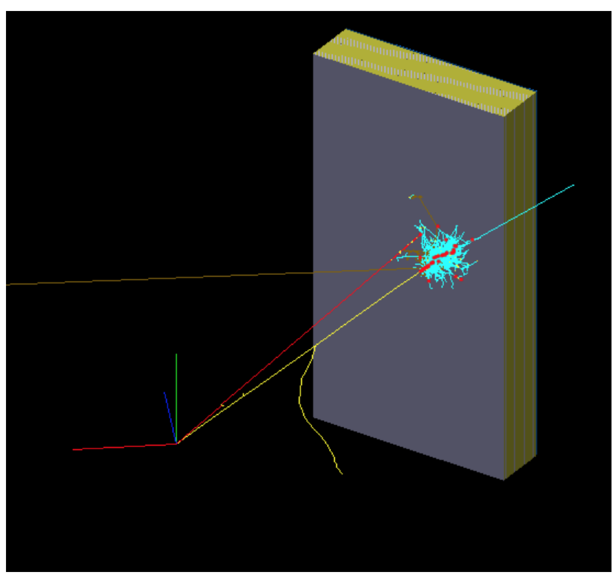

Figure 22: The LAC in the Geant4 Simulation. The red trajectory is a pion and the yellow is an electron.

However, rejection in the calorimeter for such energies will be at least a factor of 100 (when the particle momentum is used in the analysis) and the pi-to-e ratio is also reduced. Considering all of the above, the uncertainty on the pion contribution to the final event sample is expected to be on the level of 1% or less.

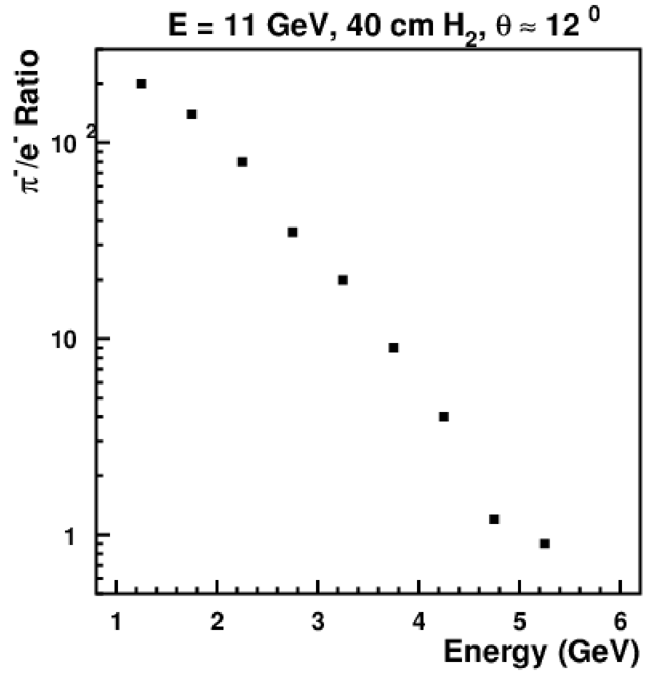

Figure 23: A pion to electron ratio in the SBS spectrometer for the hydrogen target.

2.4.2 Super Bigbite Trigger and DAQ

It is proposed that the Level-1 trigger will be formed using the total energy deposition in the LAC and the Level-2 trigger will use correlation between the coordinates of the signals in the LAC and GC-SBS and energy deposition information from two layers of LAC. The RTPC will be readout for any kind of trigger.

Pipeline Electronics For the SBS experiment GEP the proton trigger is achieved digitally using the Jefferson Lab Lab pipeline electronics. All of the 288 channels of the hadron calorimeter (HCAL) are continuously sampled at 250 MHz. The data of each block is sent to a crate trigger processor where the clustering algorithm computes the sums of 16 adjacent blocks and produces a trigger if one cluster is above threshold. This process takes about 700 ns. Once the trigger is generated, the data from the FADC is looked back up in the pipeline memory to be read out. Since the LAC has only 216 channels we propose to reuse the ECAL trigger electronics and readout to generate the single shower trigger. The singles shower trigger will also be prescaled in order to study the Cherenkov counter efficiency. The 288 channels of HCAL would require two crates with multiplexed analog signals in the overlap region.

Large Angle Calorimeter The Large Angle Calorimeter is constituted of layers of scintillator and lead. For this experiment the sensitive area will be limited to 1.8m x 3.6m to match the SBS acceptance. The detector is arranged in two parts, the front part containing 16 layers and the back part containing 17 layers. This corresponds to a total number of 256 PMTs. For the LAC PMTs summing we plan to reuse electronics of the ECAL calorimeter (an electron arm of the GEP experiment). The energy deposited in two layers of the calorimeter will be estimated by summed signals of adjacent paddles. First, we produce the overlapping sums in the both layers. It would be 58 signals for the layer-1 and 58 for the layer-2. Then the signals of two layers will be combined. The resulting 19(X) + 39(Y) analog signals will be discriminated and form (via logical OR) a Level-1 trigger. These 58 logical signals will be used in the FPGA scheme for geometrical matching of the pulses in GC-SBS and LAC as a part-1 of the Level-2 trigger. The 19 analog signals from each layer will be analyzed by using the three FADC modules for suppression of the charge pion events as a part-2 of the Level-2 trigger.

SBS Cherenkov Detector In order to suppress the trigger rate originated by pions and photons, we are planning to modify the RICH counter under commissioning for the SBS transversity experiment. It will require removal the aerogel (or blocking light from it) and substituting with CO_2 and using it as a threshold Cherenkov detector. The RICH counter has an array of 2000 PMTs as it will be used in the approved SBS transversity experiment. A 8(x2) channel amplifier discriminator board was developed by Glasgow University based on the NINO chip. Using discriminated signals provided by this board, with the amplitude over threshold of the signal integrated in the width of the logic signal, we would need 125 boards. The resulting 250 logical pulses will be used in the FPGA scheme for summed areas of geometrical match.

GEM Tracker Electronics The GEM signals for the multiple SBS tracking planes will be read using the APV25 readout and the SRS system as described above. This will be used for the RTPC in the same way that it is currently planned for the GEM trackers of Super Bigbite.

2.5 Simulations of the Radial Time Project Chamber

The impact of beam-related background processes on the RTPC operation has been assessed using a simulation based on a recent release of Geant-4 (4.10.0.p03) [71]. The simulation considers (Fig. 24) a "straw" target of radius 5 mm and length 400 mm, held in a 10 μm thick Al cylinder, with 20 μm Al end windows, and filled with 1 atm of H_2 or D_2 gas. This cell is surrounded by the He gas of the RTPC, at a pressure of 0.15 atm, contained within a volume of 150 mm radius. Both the straw target and the He volume are maintained at a temperature of $77°K$.

A ring of 127 μm radius, gold-plated Al field wires divides the He volume into an insensitive region (He-inner) at radii $r < 50$ mm and a sensitive region (He-outer) at radii $50 < r < 150$ mm. The electrons of ionization produced in He-inner region are swept to the target cell and the ions collected by the wire ring. Ionization produced in He-outer is moved by the radial electric field to an outer ($r > 150$ mm) triple GEM detector with pixel readout. Calculations have also been made for a target pressure of 2 atm and temperature 25°K which provide projected luminosity of experiment. The density of the He gas in the RTPC has been fixed at 9.75×10^{-5} g/cm^3 which corresponds to a pressure of 0.15 atm at 77°K. Essentially backgrounds have been found to scale with the thickness of the target.

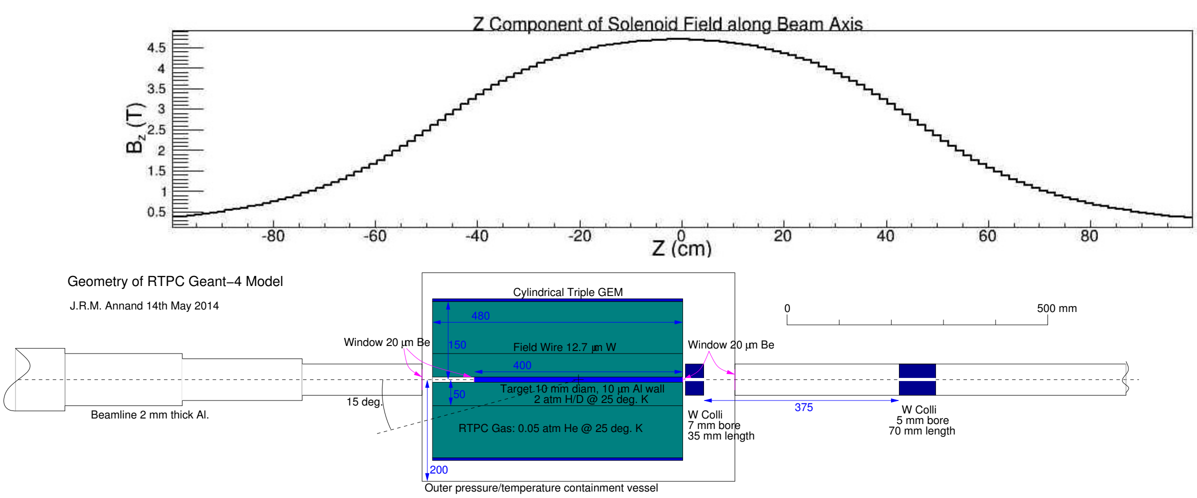

Figure 24: Top: the z-dependence of the longitudinal component of the S3 solenoid magnetic field B_z. Bottom: Geometry of the MC simulation of background processes. **Note**: the direction of the electron beam from the right to the left.

Operating with the target at 77°K and 1 atm, an electron beam current of ~ 60 μA will produce a luminosity 2.9×10^{36}cm^{-2}s^{-1}. The largest background will be observed in the vicinity of the target. This comes mainly from Møller scattering of the incident electrons, with smaller contributions from bremsstrahlung and pair production. Most of the background electrons have low energy and are confined inside the insensitive region of the RTPC (He-inner) by the solenoid magnetic field.

Figure 25(A) shows the radial distribution of energy deposited in the target and RTPC for different magnetic field strengths. The calculation has been made with 8×10^8 incident 11 GeV electrons, for uniform fields of 1.0, 2.0, and 4.0 T, as well as the "S3" solenoid

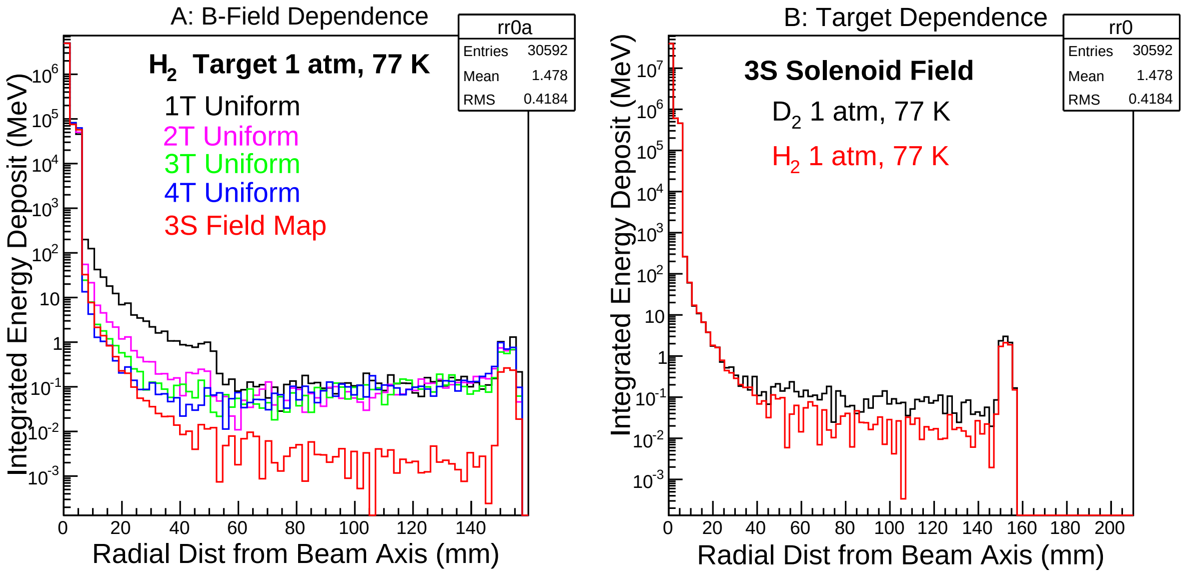

Figure 25: A: confinement of Møller energy deposit for a 1 atm, 77K target and various magnetic field configurations. B: S3 solenoid field map and different targets. Simulations have 8×10^8 incident electrons of 11 GeV energy.

field map (Fig.24) calculated in TOSCA. In the region of the target the maximum S3 longitudinal field is in excess of 4 T.

As the field strength is increased the radial rate of decrease of the energy loss becomes steeper, in the He-inner. However, there remains a background in He-outer which is not suppressed by increasing the field strength. A small fraction, $\sim 5\%$, of this can be attributed to intermediate bremsstrahlung in the target region, followed by pair production. But, most originate from interactions of the beam downstream from the target (Fig.24).

It is thus important that the magnetic field extends sufficiently in z and that the beam line has sufficiently large diameter to accommodate the increasing lateral spread in the exit beam. Note that the larger backgrounds observed with uniform fields, compared to S3, is largely due an unphysical sharp cutoff at the boundary of the uniform field.

The present calculations have been made both with the field-map centered on the target and with the field map displaced 200 mm upstream (as shown in Fig. 24). The exit beam line is stepped periodically to larger radii, traveling downstream from the target. Increasing the expansion of the exit beam line beyond that depicted in Fig. 24 has an insignificant effect on the He-outer background if an electron beam radius of 0.5 mm is used. The integrated energy loss in He-outer has some dependence on the beam-line material, but 2-4 mm thickness Al gives reasonable results. Upstream from the target a dual W collimator is installed to suppress increased background produced by an off-axis beam.

Figure 25(B) compares the radial energy distribution, calculated with the S3 field map, for 1_atm H_2 and D_2 targets. The mean energy losses per incident 11 GeV electron are given in Table 3 for a 1 atm, 77°K target. A column "$r \leq 50$ mm" gives the mean energy loss in the target and He-inner and column "$50 < r \leq 150$ mm" the mean energy loss in He-outer. There appears to be no significant penalty (in terms of electromagnetic background) from substituting Al for Be as the window material or from moving the solenoid magnet 200 mm upstream.

The MC generated data have also been analyzed on an event-by-event basis and column "Rate" of Table 3 gives the rate at a luminosity of 2.9×10^{36} $cm^{-2}s^{-1}$ of electron events in the sensitive region which produce a mean dE/dx along the track exceeding 0.1 keV/mm. Protons of interest would be expected to produce a larger dE/dx. Detectable rates in the sensitive area of 22.8 MHz and 40.8 MHz for the H_2 and D_2 targets respectively will contribute to the occupancy of the readout pads in the GEM detector, but the electron track loci are quite different from those produced by protons .

Target	Mean E_{dep} (MeV)	Mean E_{dep} (MeV)	Rate
	$r \leq 50$ mm	$50 < r \leq 150$ mm	(MHz)
H_2	0.0509	0.377×10^{-8}	22.8
D_2	0.0509	0.831×10^{-8}	40.8

Table 3: Electromagnetic background calculations for H_2 and D_2 targets operated at 1 atm and 7K. The magnetic field is S3 solenoid offset by 200 mm, as in Fig. 24. The target windows are 20 μm Al.

Figure 26 compares the transverse distribution of energy deposited by secondary electrons (A) and protons (B). In the panel A, outside of the central region, there are ~ 5 tracks which would reconstruct as originating from the target, with a radius of curvature consistent with $p \sim 250$ MeV/c and negative charge. The outer ring of energy deposit is from photon conversion in the GEM detector. In B the photo proton tracks originate from the target region. For the deuterium target relatively large numbers of low momentum protons are produced as shown by the tightly curved tracks of radius a few cm.

Although electromagnetic processes are the dominant, potential source of background, electrons are effectively contained by the solenoid field and those impinging on the He-outer sensitive region generally have a relatively low dE/dx, compared to the low-momentum protons of interest to recoil tagging. Photo nuclear processes, on the other hand, have much lower cross sections, but at small electron scattering angles the high flux of quasi-real photons will produce large numbers of highly-ionizing protons in a similar momentum range to those of interest. Protons of momentum above ~ 50 MeV/c will reach the He-outer sensitive region.

Calculations of the momentum spectrum and angle dependence of photo protons was made using parametrized models. Code based on a fit to SLAC photo nuclear data [69] has commonly been used at JLab to calculate hadronic backgrounds produced in DIS. However the kinematic region spanned by the "Wiser fit" does not extend to the low momenta of interest here. The present calculations are largely based the EPC code [74], and model of various photonuclear processes for the materials in the path of the electron beam:

- ^{1}H: elastic e-p scattering has been calculated (not in EPC) from the Mott cross section and the Kelly parametrization [75] of the Sachs form factors.

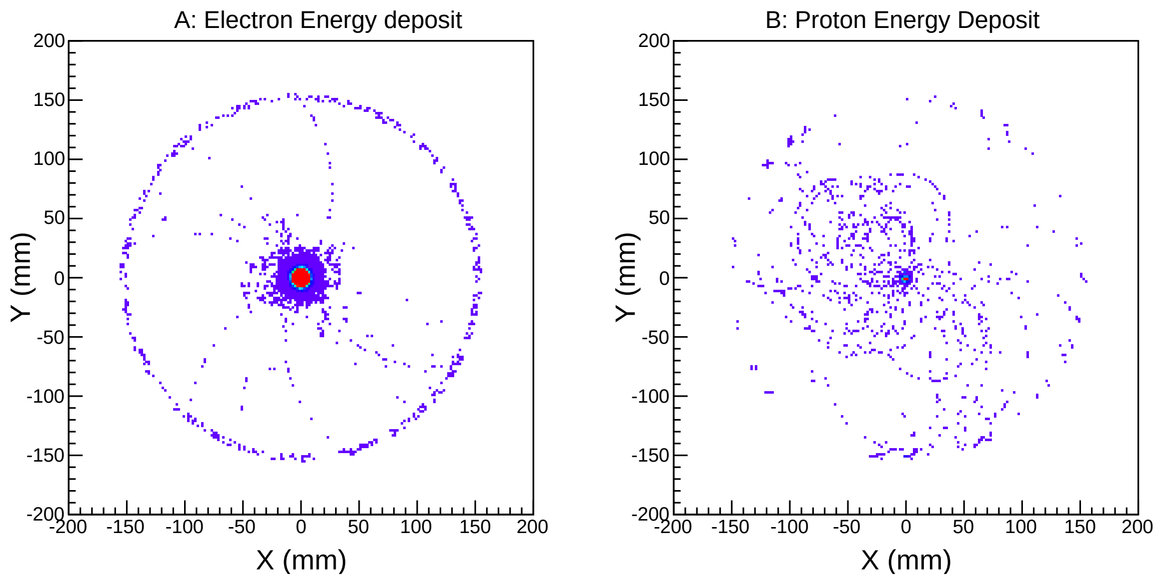

Figure 26: A: radial dependence of integrated energy loss for electrons, B: for photo protons.

- ^{2}H and ^{27}Al: nucleon recoil after quasi-free electron scattering.
- ^{2}H and ^{27}Al: deuteron (or quasi-deuteron) photodisintegration by quasi-real photons.
- ^{1}H, ^{2}H and ^{27}Al: recoiling nucleons after pion photoproduction via Δ excitation.

EPC is quoted [74] as valid for 0.5 - 5 GeV electrons, but its predictions compare reasonably with forward angle charged particle production by an 18 GeV electron beam at SLAC. It was used to generate a grid of cross section values $\sigma(p_p, \cos\theta_p)$, $p_p = 50 - 1000$ GeV/c, $\cos\theta_p = -1.0 - +1.0$, which were stored in a ROOT 2D histogram incorporated into the Geant-4 RTPC model. Photo proton events were generated by sampling p_p and $\cos\theta_p$ randomly, using the 2D histogram, and then tracked through the Geant-4 model of the RTPC. The 3S field map was employed.

Fig. 27 displays the angle and momentum dependence of photo proton intensity for ^{1}H and ^{2}H targets. Relative to ^{1}H, ^{2}H produces large numbers of low momentum protons and this intense background extends to all angles. The dark rectangles indicate the kinematic region of interest for recoil tagging. Fig. 28 compares the momentum dependence of the rate of photo protons produced in the ^{1}H and ^{2}H targets, at a luminosity of $2.9 \times 10^{36}\ cm^{-2}s^{-1}$, integrated over angle ranges of interest for TDIS. Both Fig. 28 and 27 refer to protons which reach the sensitive He-outer region of the RTPC. Histograms have been filled using reconstructed values of $p_p, \cos\theta_p$ on arrival at He-outer.

Table 4 gives the proton rates in the sensitive region of the RTPC, computed using the procedure described above, at a luminosity of 2.9×10^{36}. For ^{2}H The high rates at low momentum are mainly due to quasi-free scattering and quasi-deuteron processes. For ^{1}H the cuts in angle remove elastic scattering events and the remaining rate arises from pion

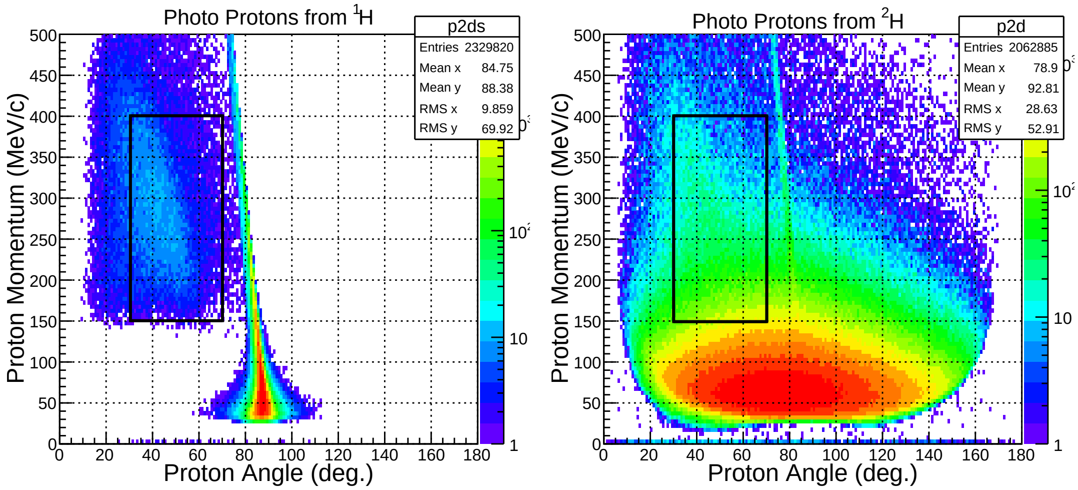

Figure 27: Comparison of momentum and angle dependence of photo protons produced in H_2 and D_2 targets and detected in He-outer. The targets were at 1 atm, 77°K. The rectangles denote the kinematic regions of interest for recoil tagging.

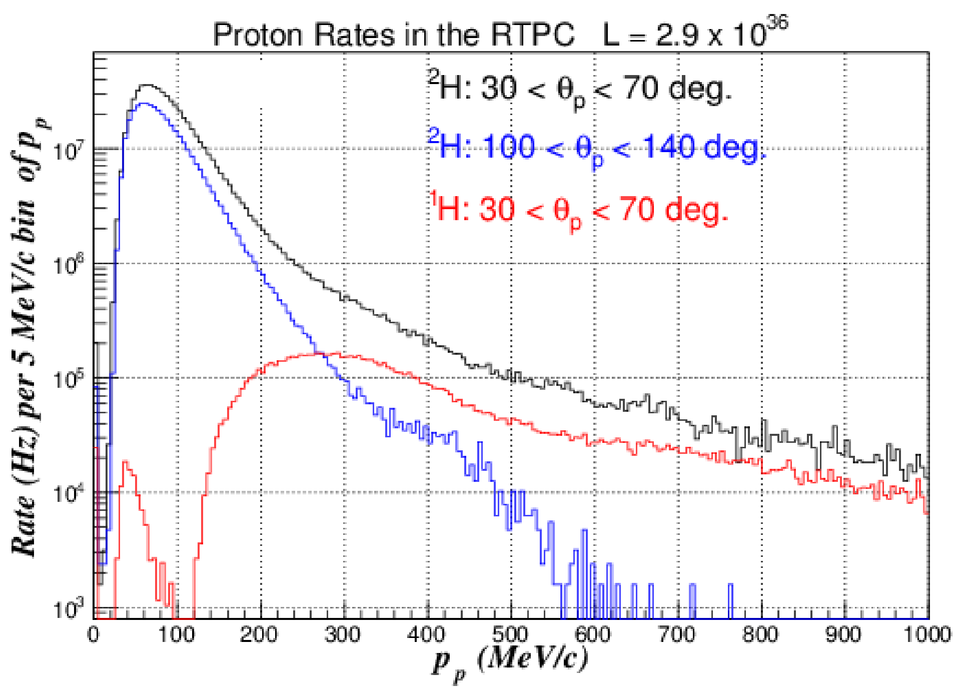

Figure 28: Rate dependence on momentum for protons produced in ^1H and ^2H targets by photo nuclear processes and detected in He-outer. Black: ^2H, proton angle range 30 - 70°. Blue: ^2H, proton angle range 100 - 140°. Red: ^1H, proton angle range 30 - 70°. The luminosity is $2.9 \times 10^{36}\ cm^{-2}s^{-1}$.

photoproduction. For the ^{27}Al windows, after a vertex cut to remove events reconstructed as originating < 10 mm from the windows, the predicted rates in the kinematic regions of interest are relatively small.

Target	θ_p (deg.)	$70 < p_p < 250$ (MHz)	$p_p > 250$ (MHz)	$150 < p_p < 400$ (MHz)
^{1}H	30 - 70	2.3	7.4	6.3
^{2}H	30 - 70	357	20.1	64
^{2}H	100 - 140	204	3.1	–
^{27}Al	30 - 70	0.37	0.0	0.05
^{27}Al	100 - 140	0.10	0.0	–

Table 4: Proton Rates in the sensitive region of the RTPC after cuts have been made on proton angle and proton momentum.

Particle Identification Analysis of step-by-step information along particle tracks produced by the simulation have been analyzed to determine dE/dx in the RTPC gas for p, π^+, K^+, e. Particles have been produced at angles $\theta = 30 - 70°$, at position $z = 0.0 \pm 5$ mm, and at momenta p_{inc} of 100 ± 1, 250 ± 1 and 400 ± 1 (MeV/c). Fig.29 displays the resulting distributions at 250 MeV/c, for tracks with a total length greater than 50 mm. The dotted line shows the position of the cut used to select proton events. Mean and rms values for dE/dx distributions are given in Tab. 5, along with the particle acceptance after the conditions $dE/dx > 0.5, 0.09, 0.05$ keV/mm for $p_{inc} = 100,\ 250,\ 400$ MeV/c respectively have been applied. These thresholds lead to a K^+ acceptance fraction of 1%.

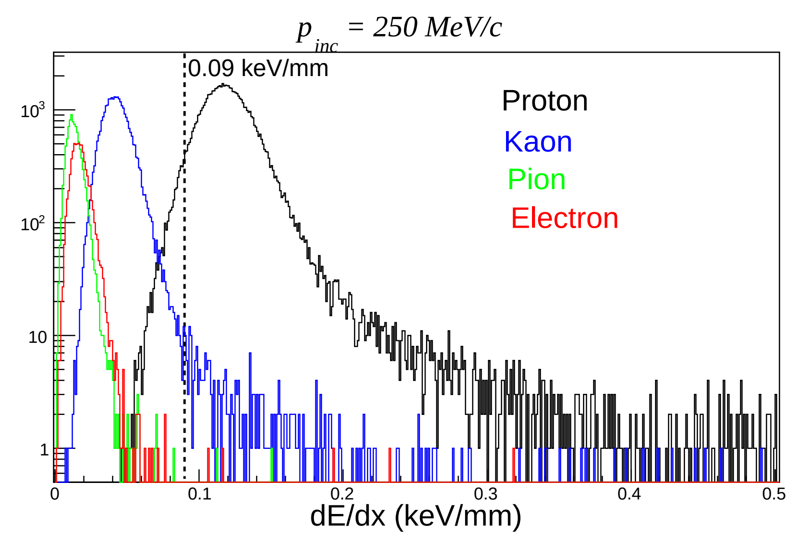

Figure 29: dE/dx for particles of momentum 250 MeV/c detected in the outer He volume of the RTPC.

Particle	p_{inc} (MeV/c)	dE/dx Thresh. (keV/mm)	p	κ^+	π^+	e
Mean dE/dx (keV/mm)	100	–	0.666	0.202	0.030	0.019
RMS dE/dx (keV/mm)	100	–	0.130	0.046	0.008	0.006
Acceptance Factor (%)	100	0.5	100	1.0	0.04	0.00
Mean dE/dx (keV/mm)	250	–	0.122	0.044	0.014	0.018
RMS dE/dx (keV/mm)	250	–	0.028	0.012	0.005	0.006
Acceptance Factor (%)	250	0.09	95.5	1.0	0.02	0.07
Mean dE/dx (keV/mm)	400	–	0.057	0.024	0.012	0.018
RMS dE/dx (keV/mm)	400	–	0.015	0.008	0.005	0.006
Acceptance Factor (%)	400	0.05	68.2	1.0	0.19	0.22

Table 5: Particle-detection mean and rms dE/dx and acceptance after a cut on dE/dx has been applied.

2.5.1 Kinematics

The kinematics reach of the experiment was studied using an event generator built for the Geant4 Monte Carlo simulation. The event generator used a flat distribution in $E_{e'}$ from $0 - 11.0$ GeV, and a flat distribution in $\theta_{e'}$ from 5 to 45 degrees and $\phi_{e'}$ of $\pm$ 12 degrees, governed by the SBS acceptance. The x_{bj} and the Q^2 is then calculated for the generated electrons. For the initial nucleon, the generator started with a proton at rest in the case of the ^{1}H target target and a neutron with initial momentum based on the momentum distribution inside the Deuteron, in the case of the ^{2}H target. The transverse momentum, P_T and $z_p = \frac{q \cdot P'}{q \cdot P}$ of the recoil proton was generated with a flat distribution between 50 - 500 MeV/c and 0 - 1, respectively and a flat ϕ distribution across 2π. Finally the momentum and scattering angle of the recoil proton (s), the t, y and $x_\pi = x_{bj}/(1 - z_p)$ were calculated for the generated events. The DIS cross section is calculated as a function of x_{bj} and Q^2 using the proton/neutron parton distributions functions in CERNLIB. The TDIS cross section was calculated using the phenomenological pion structure function described in Appendix A and using the relation $\sigma_{TDIS} = \sigma_{DIS} \times (f_2^{\pi N}/f_2^p)$.

Figs. 30 and 31 show the projected kinematics of the proposed experiment for Hydrogen and Deuterium targets, where all plots have been weighted by the TDIS cross section. As noted earlier, the x range is determined by the low t range of interest, through the variables z_p and the low spectator momentum. This x range is, moreover, optimized for observation of pions events in the meson cloud. Once the x range is fixed, the Q^2 range obtainable with the 11 GeV beam is also determined. While the latter is not very high, the kinematics are nonetheless clearly in the deep inelastic scattering regime – with W^2 values typically between 9 and 16 GeV^2.

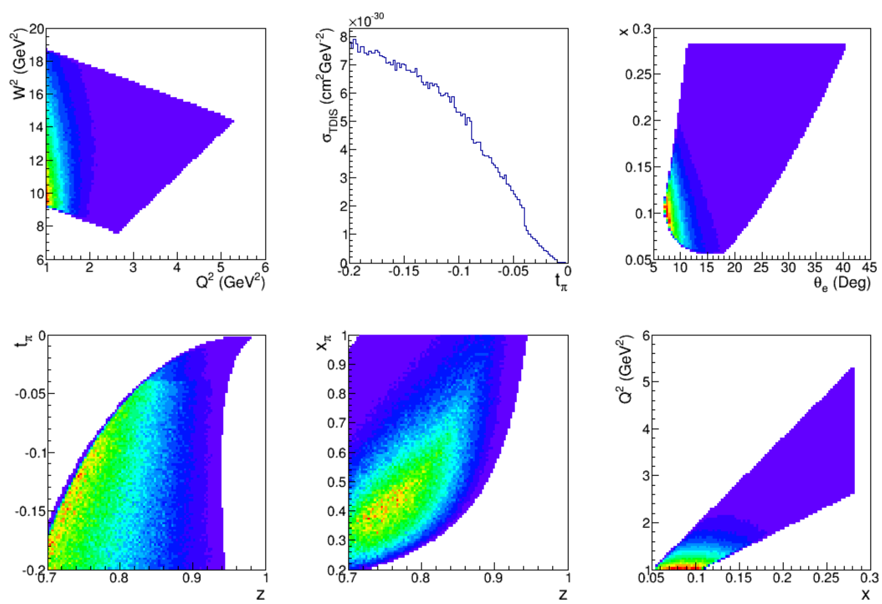

Figure 30: Kinematic coverage weighted by the TDIS cross section for a Hydrogen target.

Figs. 32 shows the projected momentum and angular range of the recoil proton for the Hydrogen target and the Deuterium target. All plots have been weighted by the TDIS

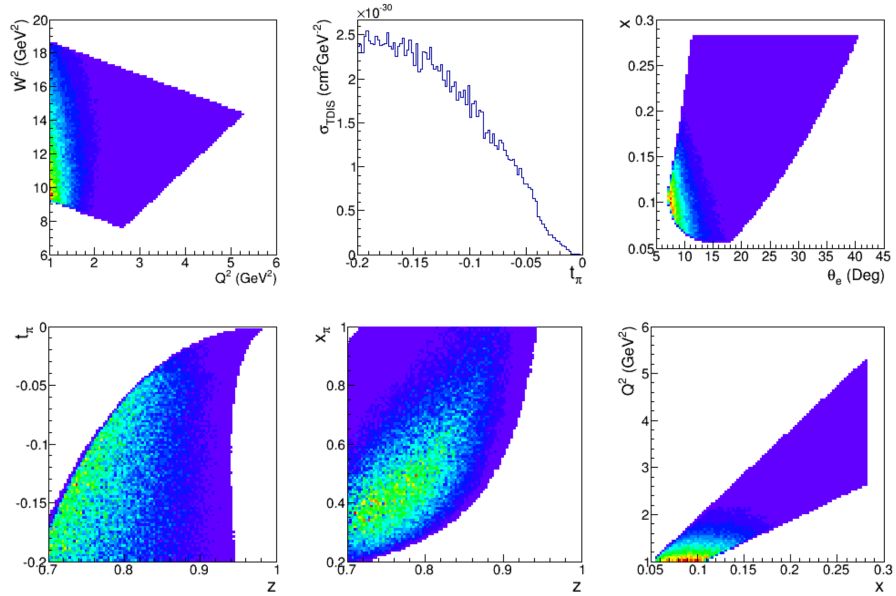

Figure 31: Kinematic coverage weighted by the TDIS cross section for a Deuterium target.

cross section.

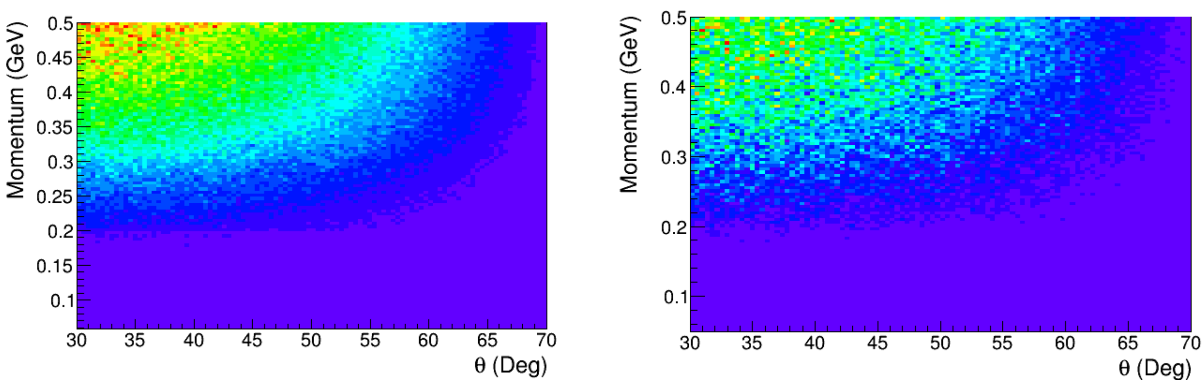

Figure 32: Recoil proton momentum vs angle weighted by the TDIS cross section, for the Hydrogen (left) and the Deuterium (right) targets.

In Figs. 33 and 34 we have shown the TDIS yield in x vs z_p bins for 10 days of beam on a Hydrogen and a Deuterium target. As described in Sec. 3.1, the beam time request is based on being able to collect $\sim 1\%$ statistics (after accounting for backgrounds) in the x, z_p bin with the lowest yield.

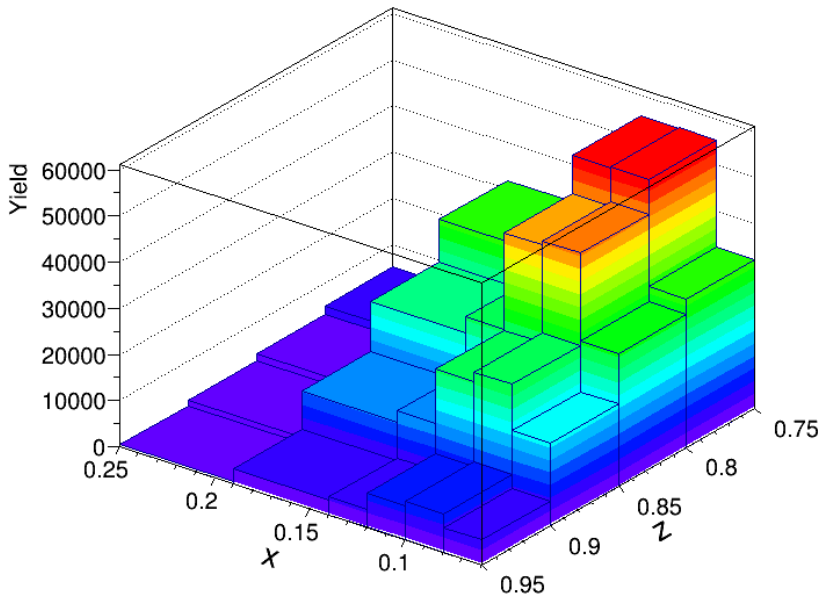

Figure 33: TDIS yields in x, z_p bins with 10 days of beam on the Hydrogen target.

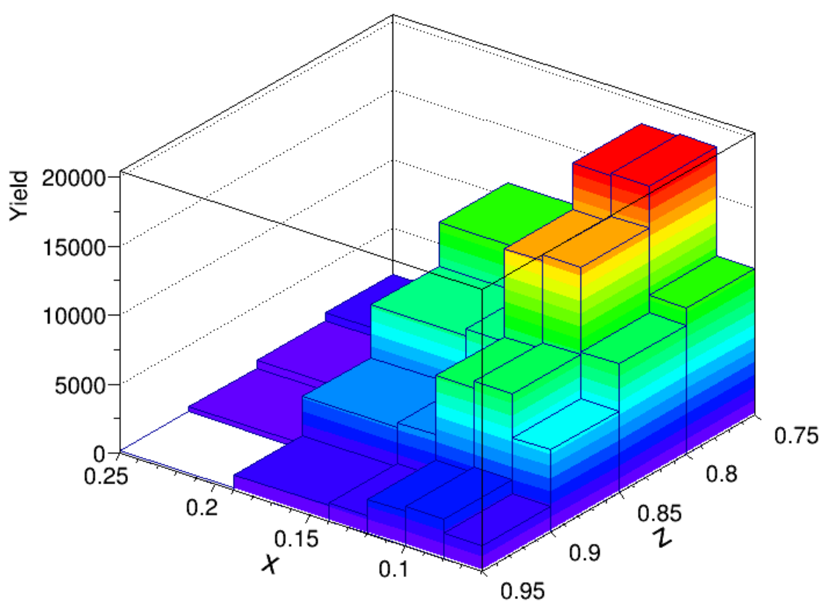

Figure 34: TDIS yields in x, z_p bins with 10 days of beam on the Deuterium target.

3 Projected Results

Fig. 35 shows the ratio of semi-inclusive structure function $F_2^{(\pi p)}(x, \Delta|\mathbf{k}|, \Delta\theta_{p'})$ to the inclusive nucleon structure function F_2^p for the neutron (left) and proton (right) and with projected data from this proposal added. The statistical uncertainty on the projected data is between 12% and less than 0.5% with the larger error being at the smallest cross section values where $F_2^{(\pi p)}(x, \Delta|\mathbf{k}|, \Delta\theta_{p'})$ dramatically turns down in x. The data will be binned in both x and proton momentum bins.

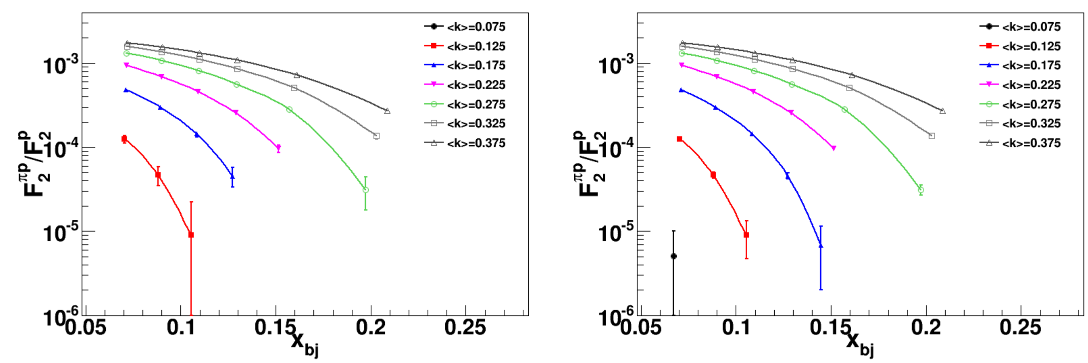

Figure 35: x dependence of the ratio of the semi-inclusive structure function $F_2^{(\pi p)}(x, \Delta|\mathbf{k}|, \Delta\theta_{p'})$ to the inclusive nucleon structure function F_2^p for the neutron (left) and proton (right). The solid curves follow from varying the integration range of $\Delta|\mathbf{k}|$, they correspond to; $\Delta|\mathbf{k}| = [60, 100]$ MeV (black), $\Delta|\mathbf{k}| = [100, 150]$ MeV (red), $\Delta|\mathbf{k}| = [150, 200]$ MeV (blue), $\Delta|\mathbf{k}| = [200, 250]$ MeV (magenta), $\Delta|\mathbf{k}| = [250, 300]$ MeV (green), $\Delta|\mathbf{k}| = [300, 350]$ MeV (light grey), and $\Delta|\mathbf{k}| = [350, 400]$ MeV (grey). The points are projections for this experiment.

Using the momentum bins of Fig. 35, Fig. 36 depicts the potential reach in t of $F_2^{(\pi p)}(t, \Delta x)$ towards the pion pole for a number of different x bins. Here, the low momentum reach of the RTPC detector is critical to define the downward-turning shape of the curve.

Fig. 37 is similar to Fig. 6, presenting the same structure function quantities for the neutron as were just shown for the proton, but with a comparison instead to the strength of other physics channels, the tagged structure functions for $(\pi^- p)$, $(\rho^- p)$, and $(\pi^0\Delta^0 + \pi^-\Delta^+)$, rather than to the measured momentum range components. The statistical uncertainty on the projected data is included, and ranges between 0.4 and 1.3%, with the larger error being at the smaller cross section, larger x values. Here, a momentum range from $250 - 400$ MeV only is shown rather than the full requested range down to 150 MeV/c. It is not anticipated that we will measure below 150 MeV/c, due to the increased background constraints. The expected statistical uncertainty for the deuterium measurement in the momentum bin $150 < k < 200$ MeV/c is 15%, moving to nearly $\sim 1\%$ in the highest momentum bin. As with the hydrogen data, multiple bins in both momentum and x will be obtained.

The proposed experiment will provide access to the pion structure function via the Sullivan process, where the coincidence of the DIS-scattered electron and the low momen-

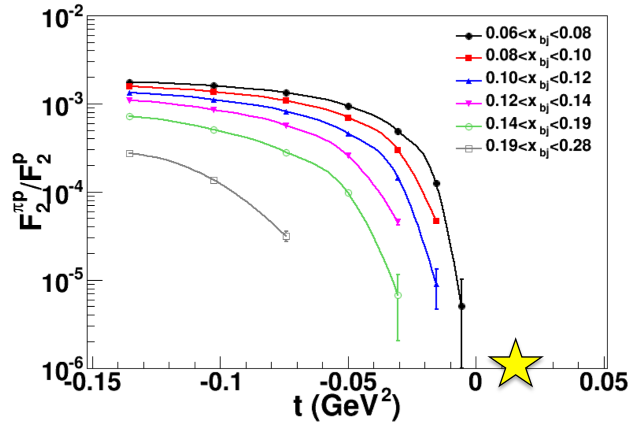

Figure 36: t dependence of the ratio of $F_2^{(\pi p)}(t, \Delta x)$ to F_2^p for momentum between 150 and 400 MeV/c, for a verying ranges in x, they correspond to $0.06 < x < 0.08$ (black), $0.08 < x < 0.10$ (red), $0.10 < x < 0.12$ (blue), $0.12 < x < 0.14$ (magenta), $0.14 < x < 0.19$ (green) and $0.19 < x < 0.28$ (grey). The points are projected data from this proposal with the statistical error bars included, but difficult to see on the log scale. The yellow star shows the location of the pion pole.

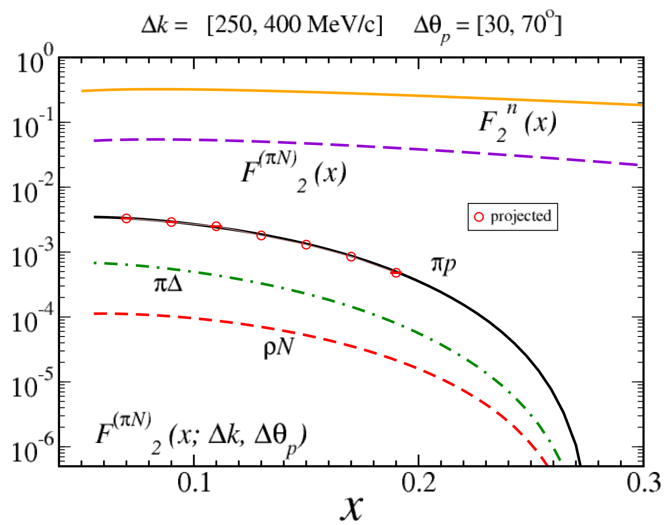

Figure 37: Structure functions as in Fig. 6 for the neutron-tagged target, with the x dependence of $F_2^{(\pi p)}(x, \Delta|\mathbf{k}|, \Delta\theta_{p'})$ for charge-exchange in, e.g., the $n \to \pi^- p$ process. The tagged semi-inclusive structure function for $(\pi^- p)$ (black, solid), $(\rho^- p)$ (red, dashed), and $(\pi^0\Delta^0 + \pi^-\Delta^+)$ (green, dot-dashed) are compared with the inclusive structure function of the neutron $F_{2n}(x)$ (orange), and the fully-integrated $(\pi^- p)$ contribution $F_2^{\pi N}(x)$ (violet, dashed). Projected data are shown, with statistical error bars included.

tum recoil proton will tag a pion target event. Experimental knowledge of the partonic structure of the pion is currently very limited due to the lack of a pion target, and most of the current knowledge of the pion structure function in the valence region is obtained primarily from pionic Drell-Yan scattering [23]-[25].

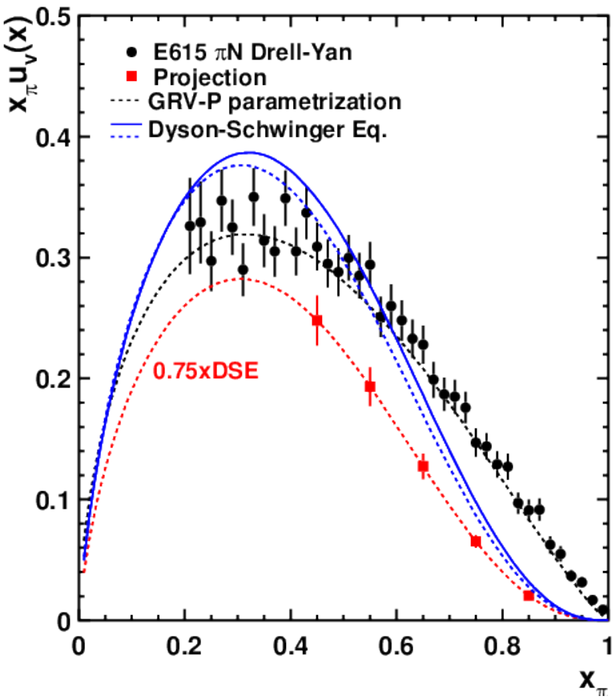

Figure 38: Projected pion structure function results. Also shown are the results from the pionic Drell-Yan experiment E615, the GRV-P parametrization and a Dyson-Schwinger equation based calculation from Ref. [26]. The projected points are shown along a curve which is 0.75×DSE, in order to demonstrate the potential for shape discrimination.

Fig 38 shows the projected pion structure function that can be extracted from this experiment. A 5% systematic uncertainty in the pion flux is assumed (to be achieved by comparing to pionic Drell-Yan data at $x_\pi = 0.5$), and a total systematic uncertainty of 8.4% is used. The projected results are shown along with the existing pionic Drell-Yan data from E615 and the GRV-p parametrization of the pion structure function, and a calculation based on the Dyson-Schwinger equation [26]. There are several theoretical calculations of the pion structure in the valence region, however they tend to disagree with each other – underscoring that it is essential to measure the pion structure function over a wide range of x.

As can be seen in Fig. 38, the proposed data nicely complement the Drell-Yan data and will fill in the heretofore unprobed moderate x range. Moreover and importantly, measurements of pion parton distributions using the Drell-Yan process are limited to charged pions, while the proposed experiment will also include the neutral pion and provide a check of the validity of isospin symmetry and any dynamical effects that differ between neutral and charged pions.

3.1 Beam Time Request

We propose to measure the semi-inclusive reactions $p(e, e'p)X$ and $D(e, e'pp)X$ using a 50μA beam on a 1 atm, cooled straw, gaseous hydrogen target with radius of 5 mm and length of 40 cm, for a total luminosity of 3×10^{36} cm^{-2}s^{-1}. The well-known DIS cross section was used as the initial basis for calculation [67], in conjunction with the rate due to the pionic contribution (from the calculations presented in Sec. 1.1) is given by:
Rate(DIS$_{\pi N}$) = Rate(DIS)$\times(F2_{\pi N}/F2_n)$.
The Tagged-DIS rate on hydrogen is given by:
Rate(TDIS$_{\pi N}$) = Rate(DIS)$\times$ eff$_{RTPC}\times$ eff$_{SBS}$,
using a conservative combined RTPC efficiency and acceptance of 40% and SBS efficiency of 90%. The x range $0.06 < x < 0.2$ will be divided into 5 bins and, for *each* bin in x, the recoil proton momentum k will be divided into at least another 6 bins. The requested beam time is estimated with the goal of better than 1% statistical uncertainty on average for the recoil momentum k bins within each x bin. The worst case scenario is the lowest rate, highest x bin, where we estimate that 10 days of beam time is needed to obtain adequate statistical precision. Due to the large acceptance of the SBS and RTPC, all of the other remaining data displayed and projected will be obtained *simultaneously* with this bin and so require no additional beam time request.

Table 6 shows the estimated electron cross section within the SBS acceptance, the $F2_{\pi N}/F2_n$, the projected TDIS rate, and the yield in each x bin for 10 days of beam on a hydrogen target. Table 6 also shows the yield in each x bin for 10 days of beam on a deuterium target. The expected statistical uncertainty for the deuterium measurement in the momentum bin $150 < k < 200$ MeV/c is 15%, moving to nearly $\sim 1\%$ in the highest momentum bin. The requirement of two low momentum protons detected in vertex and time coincidence (one backward and one more forward) requires double-accounting for the RTPC efficiency when using the deuterium target – which is very conservatively estimated here. Each kinematic E', θ, ϕ bin must pass cuts on the SBS acceptance, and an electron trigger energy < 6 GeV, and threshold > 1 GeV are required. There are also kinematic cuts employed to ensure $W > 2$ and $Q^2 > 1$ GeV^2.

Table 7 shows the estimated statistical uncertainty, $\delta\sigma/\sigma$ in percent, for the proton momentum bins (Δk, top) to be measured *within an x bin* around 0.1 ± 0.01 for the hydrogen target, as an example for the momentum range and breadth of data expected within *each* of the x bins in Table 6. The range of momentum bins will directly provide a corresponding range of t bins for each x. Here, the electron and proton yields, $N_{e,e'}$ and $N^{good}_{e,e'p}$, are subject to the same cuts and efficiency assumptions as in Table 6, above. The electron yields, $N_{e,e'}$, are based on well known DIS cross section [67], the yields for the protons of interest is estimated as $N^{good}_{e,e'p} = N_{e,e} \times (F_2^{\pi N}/F_2^p)$, the accidental proton yields $N^{acc}_{e,e'p}$, are based on the background simulation described in Sec. 2.5 and are estimated as described in Sec. 2.2.1. Finally the statistical uncertainty is estimated as $\delta\sigma = \sqrt{N^{good}_{e,e'p} \times (1 + B/S)}$, where S/B is the signal to background ratio.

In addition to 10 days of 11 GeV beam on hydrogen and 10 days on deuterium, we request also 5 days on a hydrogen target at a reduced luminosity in order to validate the background subtraction procedure. It will be necessary to commission the RTPC, the new SBS electron detection system, as well as to verify the vertex and reconstruction

x range	σ_e in SBS (nb)	$F_2^{\pi N}/F_2$ (x 10^{-5})	TDIS πN Rate (Hz)	Yield H_2 10 days (k)	Yield D_2 10 days (k)
0.06 - 0.2	1.84	116	2.31	1993	798
0.06 - 0.08	0.22	336	0.80	688	276
0.08 - 0.10	0.29	230	0.71	614	246
0.10 - 0.12	0.30	137	0.45	390	156
0.12 - 0.14	0.29	69	0.21	184	74
0.14 - 0.19	0.67	13	0.10	83	34

Table 6: Rates and expected yields for this experiment in the proposed x bins. All of the data will be obtained simultaneously for each target within the acceptance(s) of the SBS and RTPC without changing settings. Multiple proton momentum bins will be obtained within each x bin, as shown in the example below.

Δk (MeV/c) ΔT (MeV)	150-200 9	200-250 12	250-300 15	300-350 17	350-400 20
$N_{e,e'}$ ($\times 10^6$)	710	710	710	710	710
$N_{e,e'p}^{good}$ ($\times 10^3$)	59	159	267	354	413
$N_{e,e'p}^{acc}$ ($\times 10^3$)	380	510	640	724	852
S/B	1/6.4	1/3.2	1/2.4	1/2	1/2
$\delta\sigma/\sigma$ (%)	1.1	0.5	0.4	0.3	0.3

Table 7: Statistical uncertainty for this experiment in an example x bin around 0.1 ± 0.01 for the hydrogen target. It is planned that each proposed x bin will be broken down into such k bins, and that all of the data will be obtained simultaneously for each target within the acceptance(s) of the SBS and RTPC.

optics. We request 2 beam days (mixed evenly between the the hydrogen and deuterium targets), also at 11 GeV, for these requisite preparations. We note that the collaboration anticipates some advance detector pre-commissioning of the RTPC and SBS detectors using radioactive sources, cosmic rays, and possibly the low energy proton beam at TUNL as was done in advance for BONUS. Lastly, two shifts of beam time at 4.4 GeV will be required for measuring the RTPC acceptance and efficiency using elastic neutrons measured in HCAL, as described above. The two shifts are planned to take place one at the start of the deuterium running and one at the end to track any time-dependent systematic effects. This will require two half-shift beam energy changes, where target gas changes will take place concurrently. The total beam time request of 27 days is summarized in Table 8.

Target	Current (μA)	Beam Energy (GeV)	Beam Time (hrs)	Notes
Hydrogen	50	11	240	includes 1 day for commissioning
Deuterium	25	11	240	includes 1 day for commissioning
Hydrogen	5	11	120	
Deuterium	5	4.4	48	RTPC calibration with HCAL
			8	Beam Energy Changes
Total			656	27 days

Table 8: Summary of beam time request.

3.2 Expected Experimental Accuracy

An overall systematic uncertainty of 5% in the cross section measurements is assumed for this experiment, building on the CLAS-6 BONUS and eg6 experience utilizing the RTPC [68]. We believe this to be highly reasonable for the following reasons. First, CLAS-6 had a large (> 5%) uncertainty associated with the E', θ dependent CLAS trigger efficiency. The SBS is a far simpler device, and is expected to have a very small trigger efficiency uncertainty and only a 3% overall systematic uncertainty. In BONUS, moreover, 4.2% of the 8.7% overall systematic uncertainty came from the inclusive F_2^d/F_2^p model dependence in the ratio measurement performed – largely in the resonance region. We are here proposing a cross section measurement, with no ratio normalization technique to be employed. SBS inclusive results can be verified against the well-known proton DIS cross section. Moreover, the better spatial resolution of the proposed GEM readout, combined with the increased drift distance, will improve tracking and vertex resolution in the RTPC as compared to BONUS. We also propose not only to use a Monte Carlo for the RTPC acceptance and efficiency, but to carefully measure it using the HCAL elastic neutron technique described above. We have analyzed the background which is due to real coincidence between the DIS electron and secondary mesons misidentified as protons. As mentioned earlier, the uncertainty on the pion contribution to the electron sample is expected to be on the level of 1% or less. Secondary mesons misidentified as protons can be determined with a 10% uncertainty, which implies a 1% uncertainty in the true coincidence counts. The anticipated impact on the systematic uncertainty due to backgrounds is expected to be small due to several available methods which are proposed to evaluate them. For example, a coincidence time cut and a vertex (δz) cut will be used. Low luminosity data taking (5 PAC days requested for these studies) will also be used to verify the simulations and calculations from the higher rate data. This is included in the systematic uncertainty table below (Table 9).

4 Summary

We propose a pioneering measurement technique for probing the elusive mesonic content of the nucleon structure function. The technique involves detecting a low-momentum

Source	Uncertainty
Accidental background subtraction	5%
DIS electron cross section (Targ. density, beam charge, acceptance, det. efficiency)	3%
RTPC absolute efficiency	2%
RTPC deadtime	1%
RTPC momentum resolution	$< 1\%$
RTPC angular acceptance	1%
Beam position	$< 1\%$
Total	6.5 %

Table 9: Table to systematic uncertainties

recoil proton (pair of protons) in coincidence with a deeply inelastically scattered electron from a hydrogen (deuterium) target. By tagging events from bound objects in the target, this technique provides a probe of the meson cloud component in the nucleon, and thereby access to the meson structure function. Additionally, this experiment will measure for the first time the tagged DIS cross section for proton and neutron targets in the target fragmentation region. The measurement will be performed in the Q^2 range of 0.5 to 6 $(\text{GeV/c})^2$ at very low proton momenta in the range of $(60 - 400)$ MeV/c. The experiment will use the Super Bigbite Spectrometer to detect the scattered electrons and a low mass radial time projection chamber (RTPC, a BONUS-like detector) to detect the low momentum proton(s) in time and vertex coincidence with a DIS electron. In this experiment a 50μ A, 11 GeV beam will be incident on a 5 mm radius, 40 mm long straw tube target with 1 atm cool hydrogen (deuterium) gas. We request a total of 22 days of beam time, with 10 days of production 50 μA beam on the hydrogen target, 5 days production on the deuterium target, 2 days for optics and detector commissioning, and an additional 5 days of 5 μ A beam on the hydrogen target for background checks.

A A Phenomenological Model of Tagged Deep Inelastic Scattering

We review the predictions of pion cloud models for contributions to the structure functions of the nucleon, firstly for the inclusive DIS case, and then to the "tagged" semi-inclusive cross sections, which we study as a function of several kinematic variables [46, 47, 48].

A.0.1 Meson Cloud Contributions to Inclusive DIS

As pointed out by Sullivan [3], the contribution to the inclusive F_2 structure function of the nucleon from scattering off a virtual pion emitted from the nucleon can be written as

$$F_2^{(\pi N)}(x) = \int_x^1 dz\, f_{\pi N}(z)\, F_{2\pi}\Big(\frac{x}{z}\Big), \tag{12}$$

where $z = k^+/p^+$ is the light-cone momentum fraction of the initial nucleon carried by the interacting pion. In the infinite momentum frame this coincides with the longitudinal momentum fraction, while in the rest frame of the target nucleon, which we will use in the following, z is expressed as $z = (k_0 + |\mathbf{k}|\cos\theta)/M$, where M is the mass of the nucleon, $k_0 = M - \sqrt{M^2 + \mathbf{k}^2}$ is the pion energy, and θ is the angle between the vector $\mathbf{k}$ and the z-axis (which is equal to the angle between the recoil proton momentum $\mathbf{p}'$ and the photon direction). For ease of notation, we also suppress the explicit dependence of the structure functions on the scale Q^2.

The function $f_{\pi N}(z)$ gives the light-cone momentum distribution of pions in the nucleon,

$$f_{\pi N}(z) = c_I \frac{g_{\pi NN}^2}{16\pi^2} \int_0^\infty \frac{dk_\perp^2}{(1-z)} \frac{G_{\pi N}^2}{z\,(M^2 - s_{\pi N})^2} \left(\frac{k_\perp^2 + z^2 M^2}{1-z}\right), \tag{13}$$

where $k_\perp$ is the transverse momentum of the pion, $g_{\pi NN}$ is the πNN coupling constant, and the isospin factor $c_I = 1$ for π^0 ($p \to p\pi^0$ or $n \to n\pi^0$) and $c_I = 2$ for $\pi^\pm$ ($p \to n\pi^+$ or $n \to p\pi^-$). The function $G_{\pi N}$ parametrizes the momentum dependence of the πNN vertex function, which, due to the finite size of the nucleon, suppresses contributions from large-$|\mathbf{k}|$ configurations. Similar expressions (though somewhat more involved) can be written for other contributions, such as from ρ mesons or with Δ baryons in an intermediate state. However, because of the small mass of the pion, the πN configuration is expected to be the dominant one. In Eq. (13) the variable $s_{\pi N} = (k_\perp^2 + m_\pi^2)/z + (k_\perp^2 + M^2)/(1-z)$ represents the total squared center of mass energy of the intermediate πN system, and is related to the pion virtuality t by $t - m_\pi^2 = z(M^2 - s_{\pi N})$.

The form factor $G_{\pi N}$ (or more generally G_{MN} for a meson M) can be constrained by comparing the meson cloud contributions with data on inclusive $pp \to nX$ scattering, as performed by Holtmann *et al.* [47]. For the purpose of this proposal, we use the parametric form

$$G_{\pi N} = \exp\left[(M^2 - s_{\pi N})/\Lambda^2\right], \tag{14}$$

where Λ is the form factor cutoff parameter. (Note that in Ref. [47] a parametrization of the form $\exp[(M^2 - s_{\pi N})/2\Lambda^2]$ is used, so that the corresponding cutoffs there are smaller by a factor of $\sqrt{2}$.) An illustration of the typical spectra for the differential cross section

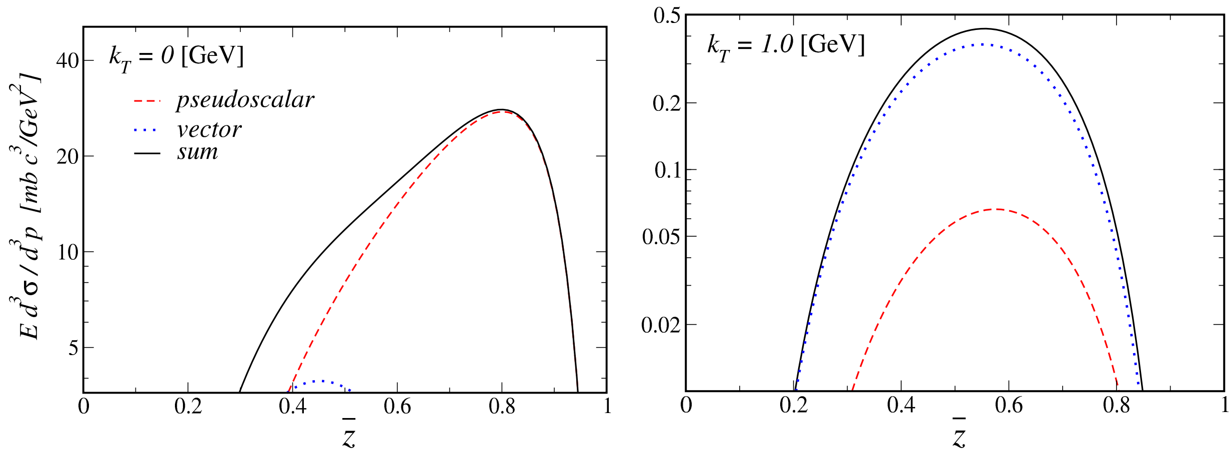

Figure 39: Typical spectra for the differential cross section $Ed^3\sigma/d^3p'$ in the $pp \to nX$ reaction for transverse momentum $k_\perp = 0$ (left panel) and $k_\perp = 1$ GeV (right panel), as a function of the light-cone momentum fraction $\bar{z} \equiv 1 - z$. The pseudoscalar π (red dashed lines) and vector ρ (blue dotted lines) contributions, and their sum (black solid lines), are indicated explicitly.

$Ed^3\sigma/d^3p'$ in the $pp \to nX$ reaction arising from π and ρ exchange is shown in Fig. 39 as a function of the light-cone momentum fraction $\bar{z} \equiv 1 - z$ carried by the final nucleon, for two values of the transverse momentum $k_\perp$. For small $k_\perp$ the π exchange contribution clearly dominates the ρ at all $\bar{z}$, while at larger momenta the contributions from heavier mesons such as the ρ become more important.

Using the cutoff parameters constrained by the inclusive hadronic $pp \to nX$ data, which were found in Ref. [47] to be $\Lambda_{\pi N} = \Lambda_{\rho N} = 1.56 \pm 0.07$ GeV and $\Lambda_{\pi\Delta} = \Lambda_{\rho\Delta} = 1.39 \pm 0.07$ GeV, the light-cone momentum distributions $f(z)$ are shown in Fig. 40. The principal model uncertainty in these results comes from the ultraviolet regulator G used to truncate the $k_\perp$ integrations in the distribution functions. Various functional forms have been advocated in the literature aside from the s-dependent exponential form factor in Eq. (14), and we compare several of these, including s- and t-dependent dipole forms, in Fig. 41. For the s- and t-dependent forms in particular, the differences are noticeable mostly at small values of z, where the t-dependent parametrization (of the form $G \sim 1/(t - \Lambda^2)^2$) tends to give somewhat larger distributions that are peaked at smaller z, compared with the s-dependent form, which tend to be broader.

Convoluting the light-cone distributions with the structure function of the meson as in Eq. (12), the resulting contributions from the πN and ρN intermediate states to the inclusive F_2 structure function of the proton is illustrated in Fig. 42. For the meson structure function we use the parametrization from GRV, and assume that $F_{2\pi}(x) \approx F_{2\rho}(x)$. The results are plotted for fixed values of the scattering angle of the final state electron θ_e, which determines the Q^2 dependence of the contribution at a given x. For angles between $\theta_e = 15^\circ$ and 40° the Q^2 dependence is rather negligible due to the mild Q^2 dependence of the meson structure function. For the fully integrated results of Fig. 42, the model uncertainties are greatest for the lowest accessible values to the proposed experiment of $x \sim 0.05$.

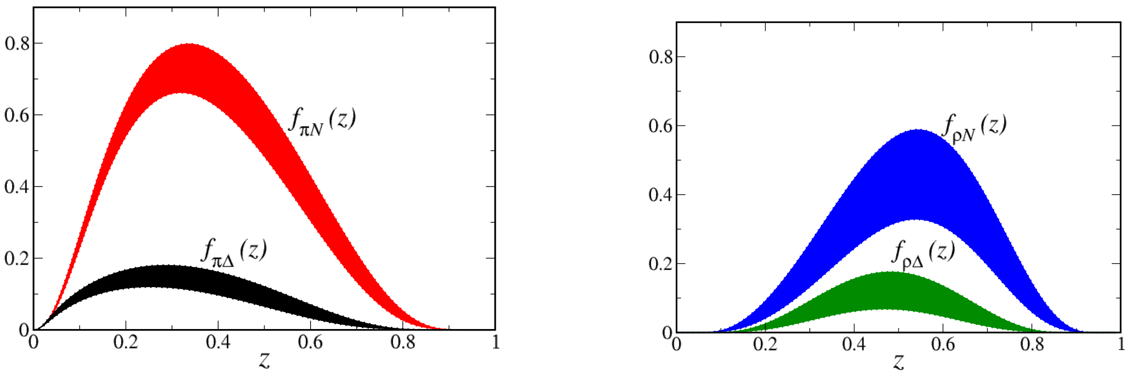

Figure 40: Light-cone momentum distributions of the pion, $f_{\pi N}$ and $f_{\pi\Delta}$ (left panel) and the ρ meson, $f_{\rho N}$ and $f_{\rho\Delta}$ (right panel), as a function of the meson light-cone momentum fraction z. The error bands correspond to the cutoff parameter ranges as given in the text.

A.0.2 Tagged Structure Functions

While the inclusive reactions require integration of the pion momentum over all possible values, detecting the recoil proton in the final state allows one to dissect the internal structure with significantly more detail and increase the sensitivity to the dynamics of the meson exchange reaction. In general, we will be interested in the relative contributions of the semi-inclusive reaction with respect to the inclusive process. In practice, the semi-inclusive structure function will be given by the unintegrated product

$$F_2^{(\pi N)}(x, z, k_\perp) = f_{\pi N}(z, k_\perp)\, F_{2\pi}\Big(\frac{x}{z}\Big), \tag{15}$$

where the unintegrated distribution function $f_{\pi N}(z, k_\perp)$ is defined by

$$f_{\pi N}(z) = \frac{1}{M^2}\int_0^\infty dk_\perp^2\, f_{\pi N}(z, k_\perp^2). \tag{16}$$

The dependence of the tagged structure functions on the kinematical variables that are measured experimentally can be studied by relating the magnitude of the 3-momentum $\mathbf{k}$ of the exchanged pion in the target rest frame to the pion's transverse momentum $k_\perp$ and light-cone fraction z,

$$\mathbf{k}^2 = k_\perp^2 + \frac{\left[k_\perp^2 + (1-[1-z]^2)M^2\right]^2}{4M^2(1-z)^2}. \tag{17}$$

Experimentally, the quantities most readily measured are the momentum of the produced proton, $\mathbf{p}'$, which in the rest frame is $\mathbf{p}' = -\mathbf{k}$, and the scattering angle $\theta_{p'} = \theta$ of the proton with respect to the virtual photon direction. In the limit $k_\perp^2 = 0$, the magnitude of $\mathbf{k}$ becomes

$$|\mathbf{k}|_{k_\perp^2=0} = \frac{zM}{2}\left(\frac{2-z}{1-z}\right), \tag{18}$$

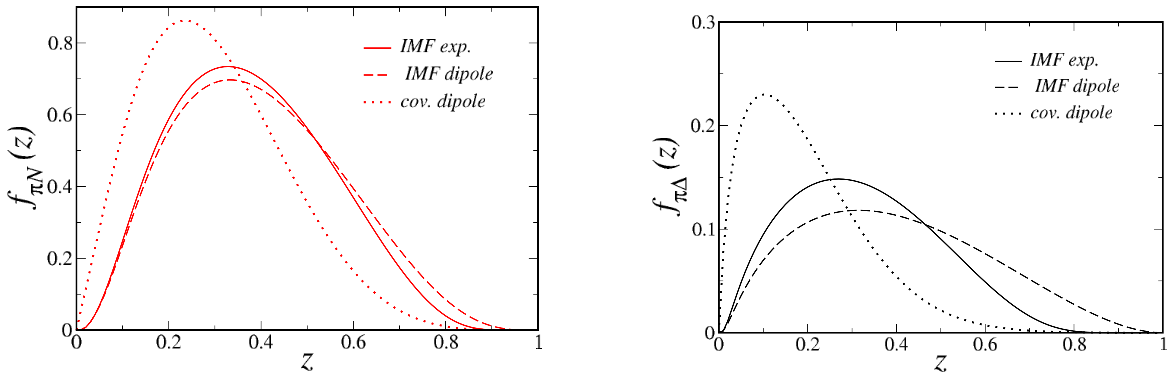

Figure 41: Light-cone momentum distributions for the πN (left panel) and $\pi\Delta$ (right panel) intermediate states, for several different functional forms of the form factor G in Eq. (13): "IMF" refers to s-dependent forms such as in Eq. (14), while "cov" denotes a form factor that depends only on the variable t.

which imposes the restriction $z \lesssim |\mathbf{k}|/M$. This relation is illustrated in Fig. 43 for values of z up to 0.2.

This is a critical guiding parameter for the proposed experiment. Since we seek to measure the low momentum region where pseudo scalar production dominates, the region of interest becomes $z \lesssim 0.2$. This corresponds to the measurable proton range, $60 \lesssim \mathbf{k} \lesssim 400$ MeV/c, of the radial time projection chamber discussed in detail below. It is important to note that, since $x < z$, this also determines both the x and Q^2 (given the maximum beam energy) of the experiment.

The kinematic restrictions on $|\mathbf{k}|$ for a given z can also be illustrated by considering the unintegrated light-cone distribution functions as a function of the variable t. This is relevant since one way of identifying the pion exchange mechanism is through its characteristic t dependence, which is pronounced near the pion pole at $t = +m_\pi^2$. The production of a physical proton (or Δ baryon) in the final state restricts the maximum value of t, however (corresponding to the minimum transverse momentum, $k_\perp = 0$), to

$$t_{\min}^{N} = -\frac{M^2 z^2}{1-z}, \qquad t_{\min}^{\Delta} = -\frac{\left(M_\Delta^2 - (1-z)M^2\right) z}{1-z}, \tag{19}$$

for nucleon N and Δ final states, respectively. Implementing these limits, the t-dependence of the distributions for π exchange with a nucleon or Δ recoil is illustrated in Fig. 44. Note that at the larger z value there is a considerable gap between the values of t at which Δ production is possible compared with N production.

Experimentally, the semi-inclusive cross sections will be measured in specific bins of recoil proton momentum $|\mathbf{p}'| = |\mathbf{k}|$ and scattering angle $\theta_{p'}$ (or equivalently z and $k_\perp$). We therefore define the partially integrated semi-inclusive structure function $F_2^{(\pi N)}(x, \Delta z, \Delta k_\perp^2)$,

$$F_2^{(\pi N)}(x, \Delta z, \Delta k_\perp^2) = \frac{1}{M^2} \int_{\Delta z} \int_{\Delta k_\perp^2} f_{\pi N}(z, k_\perp)\, F_{2\pi}\Big(\frac{x}{z}\Big), \tag{20}$$

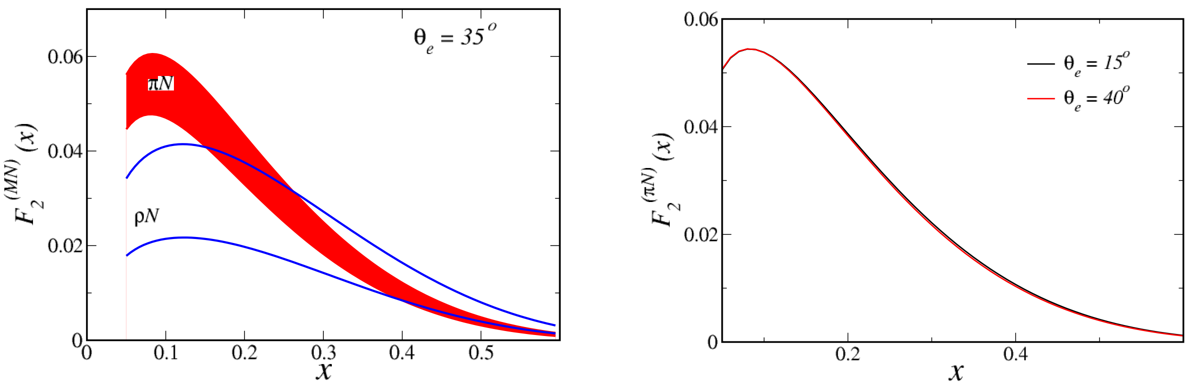

Figure 42: Contributions from πN and ρN intermediate states to the inclusive F_2 structure function of the proton for fixed electron scattering angle $\theta_e = 35°$ (left panel), and at two different angles, $\theta_e = 15°$ and $40°$ (right panel) for the πN contributions.

integrated over the range $\Delta z = [z_{\min}, z_{\max}]$ and $\Delta k_\perp^2 = [k_{\perp \min}^2, k_{\perp \max}^2]$. Alternatively, one can define an analogous semi-inclusive structure function integrated over other variables, such as $|\mathbf{k}|$ and $\theta_{p'}$, by $F_2^{(\pi N)}(x, \Delta|\mathbf{k}|, \Delta\theta_{p'})$. The proposed experiment will probe the ranges of kinematics $0.05 \lesssim z \lesssim 0.2$ and $60 \lesssim |\mathbf{k}| \lesssim 400$ MeV, and angles $30 \lesssim \theta_{p'} \lesssim 160°$, with x in the vicinity of $x \sim 0.05 - 0.2$.

Fig. 45 shows the semi-inclusive structure functions $F_2^{(MN)}(|\mathbf{k}|; \Delta x, \Delta\theta_{p'})$ for $p \to \pi^0 p$ and $p \to \rho^0 p$, as a function of the momentum $|\mathbf{k}|$, integrated over x between 0 and 0.6, and over all angles $\theta_{p'}$ from 0 to π. The structure functions rise with increasing $|\mathbf{k}|$ in the experimentally accessible region $|\mathbf{k}| \lesssim 0.5$ GeV, where The ρ contribution is clearly suppressed relative to the pion contribution. At larger momenta the effects of the meson–nucleon form factors become more important, which suppress the contributions from high-$|\mathbf{k}|$ tails of the distributions. The peak in the π distribution occurs at $|\mathbf{k}| \approx 0.6$ GeV, while the ρ distribution peaks at higher momenta, $|\mathbf{k}| \approx 1.2$ GeV, and has a slower fall-off with $|\mathbf{k}|$.

To further illustrate the capability for an experiment at the proposed kinematics to minimize effects from the $p \to \rho p$ process, Fig. 46 gives the x dependence of the semi-inclusive structure function $F_2^{(MN)}(x, \Delta|\mathbf{k}|, \Delta\theta_{p'})$ for $p \to \pi^0 p$ and $p \to \rho^0 p$, integrated over the momentum range of this experiment for all angles $\theta_{p'}$. The ρ channel is nearly two orders of magnitude smaller.

The angular dependence of $F_2^{(MN)}$ as shown in Fig. 47 again shows the dominance of the π over the ρ. The angular dependence will, moreover, prove to be important to removing the experimental background arising from low energy $e{-}p$ scattering. Elastically scattered protons in a comparable energy range to the TDIS recoil protons are essentially confined around 90°, allowing for a separation between these and the TDIS recoil protons of interest.

The effect of the pion–nucleon form factors was studied, and found to be relatively mild in this momentum interval. It is only for larger momenta ($|\mathbf{k}| \gtrsim 0.5$ GeV) that the form

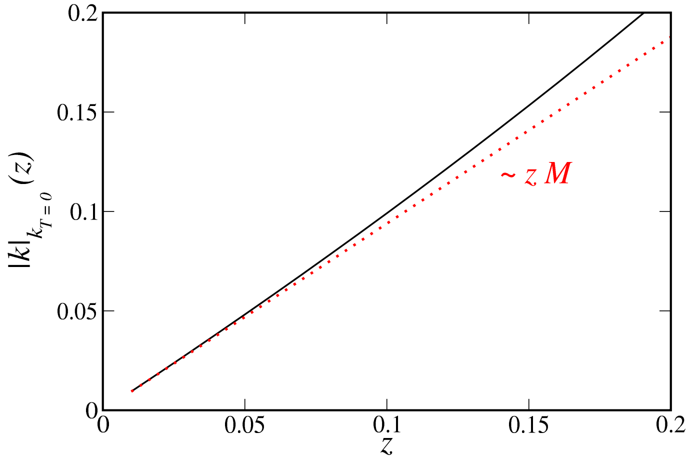

Figure 43: Pion momentum $|\mathbf{k}|$ as a function of the light-cone fraction z for $k_\perp = 0$ (black solid). The linear approximation $\sim zM$ (red dotted) is shown for comparison.

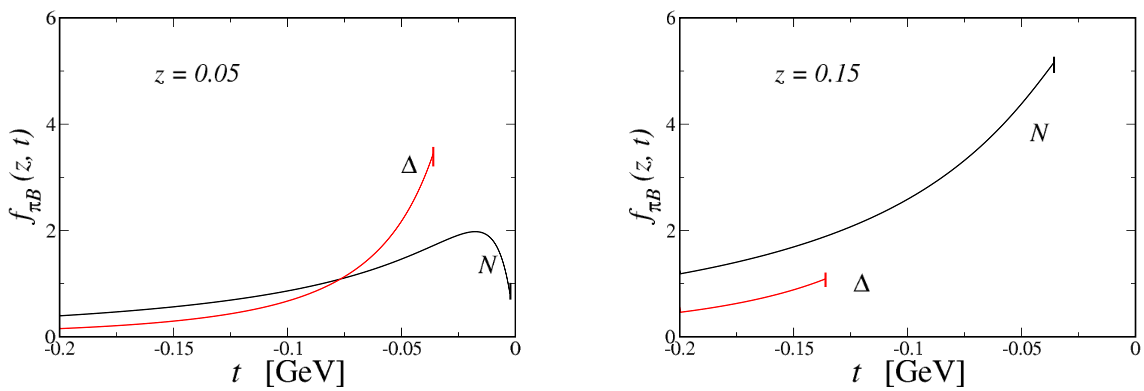

Figure 44: Unintegrated light-cone distribution functions for πN (black solid) and $\pi\Delta$ (red solid) states as a function of t, for fixed values of $z = 0.05$ (left) and $z = 0.15$ (right).

factor model becomes significant. The dependence of the semi-inclusive structure function $F_2^{(\pi N)}(x, \Delta|\mathbf{k}|, \Delta\theta_{p'})$ on the pion structure function parametrization was also studied using the GRV parametrization [77] of the pion parton distribution functions as compared with the MRS parametrization [78] with different amounts of sea, ranging from 10% to 20%. The pion structure function parameterizations are all similarly constrained by the pion–nucleon Drell-Yan data at Fermilab at intermediate and large values of x. The variation in the computed semi-inclusive proton structure function from uncertainties in the pion distribution functions is therefore smaller than the uncertainties from the pion–nucleon vertex form factor dependence.

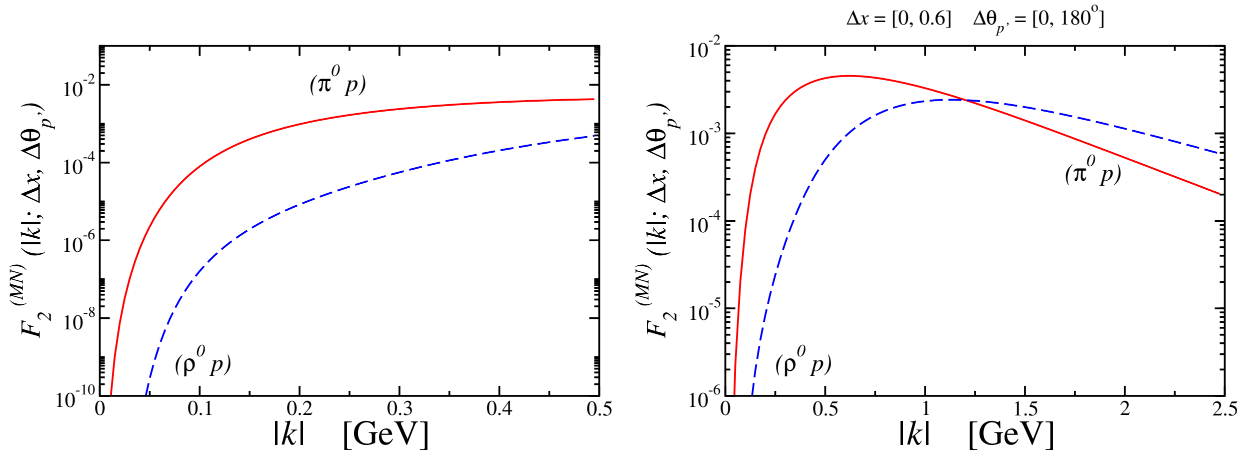

Figure 45: Semi-inclusive structure functions $F_2^{(MN)}(|\mathbf{k}|;\Delta x,\Delta\theta_{p'})$ for the $p\to M\,p$ process, with $M=\pi^0$ (red solid) and $M=\rho^0$ (blue dashed), as a function of the recoil proton momentum $|\mathbf{k}|$, integrated over $\Delta x=[0,0.6]$ and all angles $\theta_{p'}$. The left panel shows the function over the experimentally accessible range for $|\mathbf{k}|$ up to 0.5 GeV, while the right panel shows the extended range up to $|\mathbf{k}|=2.5$ GeV.

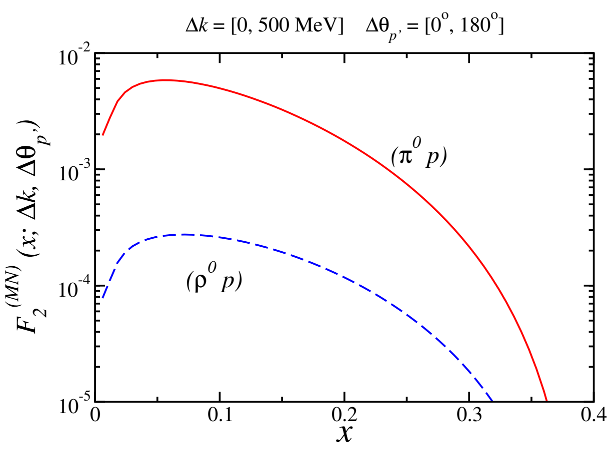

Figure 46: x dependence of the semi-inclusive structure function $F_2^{(MN)}(x,\Delta|\mathbf{k}|,\Delta\theta_{p'})$ for $p\to\pi^0\,p$ (red solid) and $p\to\rho^0\,p$ (blue dashed), integrated over the momentum range $\Delta|\mathbf{k}|=[0,500]$ MeV and over all angles $\theta_{p'}$.

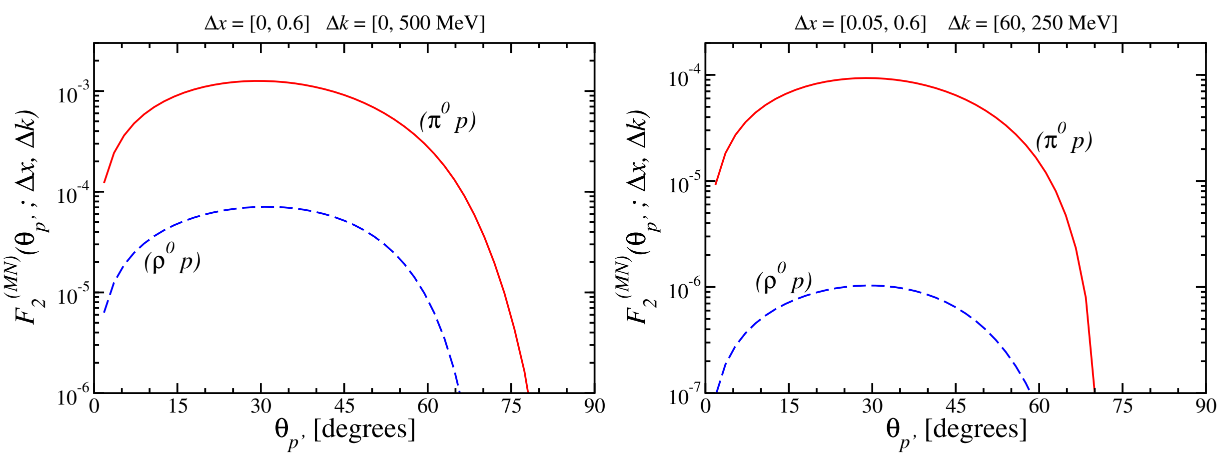

Figure 47: $\theta_{p'}$ dependence of the tagged structure function $F_2^{(\pi p)}(\theta_{p'}, \Delta x, \Delta|\mathbf{k}|)$ for neutral exchange in $p \to \pi^0\, p$ (red, solid) and $p \to \rho^0\, p$ (blue, dashed). The left panel plots the more inclusive integration ranges $\Delta x = [0, 0.6]$ and $\Delta|\mathbf{k}| = [0, 500]$ MeV, whereas the right panel show the same, but for the more constrained integration ranges $\Delta x = [0.05, 0.6]$ and $\Delta|\mathbf{k}| = [60, 250]$ MeV, appropriate for the proposed measurement.

References

[1] Frisch and Stern, Zeits. f. Physik 85, 4 (1933); Estermann and Stern, Zeits. f. Physik 85, 17 (1933).

[2] E. Fermi, L. Marshall, Phys.Rev. 72 1139-1146 (1947).

[3] J.D. Sullivan, Phys. Rev. **D5**, 1732 (1972).

[4] J. Speth and A.W. Thomas, Adv. Nucl. Phys. 24, 83 (1998).

[5] P.L. McGaughey, J.M. Moss, and J.C. Peng, Ann. Rev. Nucl. Part. Sci. 49, 217 (1999).

[6] S. Kumano, Phys. Rep. 303, 183 (1998).

[7] A.W. Thomas, Phys. Lett. 126B, 97-100 (1983).

[8] NMC Collaboration, P. Amaudruz et al, Phys. Rev. Lett. **66**, 2712 (1991); P. Amaudruz *et al.*, Phys. Rev. **D 50**, R1 (1994)

[9] K. Gottfried, Phys. Rev. Lett. **18**, 1174 (1967).

[10] A. Baldit *et al*, Phys. Lett. **B 332**, 244 (1994).

[11] E866 Collaboration, E. A. Hawker *et al.*, Phys. Rev. Lett. **80**, 3715 (1998).

[12] E866 Collaboration, J. C. Peng *et al.*, Phys. Rev. **D 58**, 092004 (1998).

[13] E866 Collaboration, R. S. Towell *et al.*, Phys. Rev. **D 80**, 3715 (1998).

[14] HERMES Collaboration, K. Akerstaff *et al.*, Phys. Lett. **B 464**, 123 (1999).

[15] F. M. Steffens and A. W. Thomas, Phys. Rev. **C55**, 900 (1997).

[16] S. Kumano, Phys. Rep. **303**, 183 (1998).

[17] J. P. Speth and A. W. Thomas, Adv. Nucl. Phys. **24**, 83 (1998).

[18] G. T. Garvey and J. C Peng, Prog. Part. Nucl. Phys. **47**, 203 (2001).

[19] R. Holt and C. Roberts, Rev. of Mod. Phy. **82**, 2991 (2010).

[20] S. C. Pieper and R. B. Wiringa, Ann. Rev., Nucl. Part. Sci. **51**, 53 (2001).

[21] R. B. Wiringa, Phys. Rev. **C73**, 034317 (2006).

[22] P. Maris, C. D. Roberts, P. C. Tandy, Phys. Lett. **B420**, 287 (1998).

[23] J. S. Conway *et al.*, Phys Rev. D **39**, 39 (1989).

[24] J. Badier *et al.*, Z. Phys. **C18**, 281 (1983).

[25] B. Betev *et al.*, Z. Phys. **C28**, 9 (1985).

[26] M. B. Hecht, C. D. Roberts, and S. M. Schmidt, Phys. Rev. **C63**, 025213 (2001).

[27] HI Collaboration, C. Adloff *et al.*, Eur. Phys. J. **C6**, 587 (1999); V. Andreev *et al.*, arxiv:1312.4821.

[28] G. R. Farrar and D. R. Jackson, Phys. Rev. lett. **35**, 1416 (1975).

[29] X. Ji, J.-P. Ma, and F. Yuan, Phys. Lett. **B610**, 247 (2005).

[30] S. J. Brodsky, M. Burkardt, and I. Schmidt, Nucl. Phys. **B441**, 197 (1995).

[31] P. Maris and C. D. Roberts, Int J. Mod. Phys. **E12**, 297 (2003).

[32] J. C. R. Bloch, C. D. Roberts, S. M. Schmidt, A. Bender, and M. R. Frank Phys Rev. **C60**, 062201 (1999).

[33] J. C. R. Bloch, C. D. Roberts, and S. M. Schmidt, Phys Rev. **C61**, 065207 (2000).

[34] T. Frederico and G. A. Miller, Phys. Rev, **D50**, 210 (1994).

[35] A. Szczepaniak, C.-R. Ji, and S. R. Cotanch, Phys. Rev. **D49**, 3466 (1994).

[36] T. Shigetani, K. Suzuki, and H. Toki, Phys. Lett. **B308**, 383 (1993).

[37] R. M. Davidson, and E. Ruiz Arriola, Phys. Lett. **B348**, 163 (1995).

[38] H. Weigel, E. Ruiz Arriola, and L. P. Gamberg, Nucl. Phys. **B560**, 383 (1999).

[39] W. Bentz, T. Hama, T. Matsuki, and K. Yazaki, Nucl. Phys. **A651**, 143 (1999).

[40] S. D. Drell, and T.-M. Yan, Phys. Rev. Lett **24**, 181 (1970).

[41] G. B. West, Phys. Rev. Lett. **24**, 1206 (1970).

[42] W. Melnitchouk, Eur. Phys. J. **A17**, 223 (2003).

[43] K. Suzuki and W. Weise, Nucl. Phys. **A634**, 141 (1998).

[44] Nikolaev *et al.*, Phys. Rev. **D60**, 014004 (1999).

[45] See, for example, Hall A PR01-110 and Hall B LOI-01-001.

[46] T. J. Hobbs et al., "A study of fracture functions for semi-inclusive electroproduction of low-momentum baryons" (2014, in preparation), arXiv:1411.2216.

[47] H. Holtmann, A. Szczurek and J. Speth, Nucl. Phys. **A 596**, 631 (1996).

[48] W. Melnitchouk and A. W. Thomas, Z. Phys. A **353**, 311 (1995).

[49] Z. F. Ezawa, Nuovo Cim. **A 23**, 271 (1974).

[50] L. Chang, C. Mexrag, H. Moutarde, C. D. Roberts, J. Rodriguez-Quintero, P. C. Tandy, Phys. Lett. **B420**, 267 (2014).

[51] C. Merzag, L. Chang, H. Moutarde, C. D. Roberts, J. Rodriguez-Quintero, F. Sabatie, S. M. Schmidt, arXiv:1411.6634, Phys. Lett. **B741**, 190 (2015).

[52] C. D. Roberts, private communication.

[53] B.Z. Kopeliovich, I.K. Potashnikova, B. Povh, Ivan Schmidt, Phys.Rev. **D85**, 114025 (2012).

[54] Yu. M. Kazarinov *et al.*, Sov. Phys. JETP **43**, 598 (1976).

[55] U. D' Alesio and H. J. Pirner Eur. Phys. J. A **7**, 109 (2000).

[56] V. Stoks Nucl. Phys. A **629**, 205c (1998);V. Stoks and Th. A. Rijken, Phys. Rev. C **59**, 3009 (1999).

[57] K. Golec-Biernat, J. Kwiecinski and A. Szczurek, Phys. Rev. **D56**, 3955 (1997).

[58] B. Kopeliovich, B. Povh and I. Potashnikova, Z. Phys. **C73**, 125 (1996).

[59] K.A. Olive *et al.* (Particle Data Group), Chin. Phys. **C38**, 090001 (2014).

[60] T. Hobbs, W. Melnitchouk, private communication

[61] F. Sauli, Nucl. Instrum. Meth. **A386**, 531 (1997).

[62] Gianfranco Morello, talk at Exploring Hadron Structure with Tagged Structure Functions workshop at Jefferson Lab (2014).

[63] S.K. Das *et al.*, Nucl. Instrum. Meth. A **625**, 39-42 (2011).

[64] A. Sharma and F. Sauli, Nucl. Instrum. Meth. A **334**, 420 (1993); Y. Assran and A. Sharma, Arxiv:1110.6761 (2011).

[65] M. J. French *et al.*, Nucl. Inst. and Meth. **A466**, 359 (2001).

[66] Dead-timeless Read-out Electronics ASIC for Micromegas.

[67] L. W. Whitlow, E. M. Riordan, S. Dasu, S. Rock and A. Bodek, Phys. Lett. B **282**, 475 (1992).

[68] S. Tkachenko *et al.* [CLAS Collaboration], Phys. Rev. C **89**, 045206 (2014).

[69] D.E. Wiser, Ph.D. Thesis, University of Wisconsin-Madison (1977) (unpublished).

[70] B. A. Mecking *et al.*, Nucl. Inst. and Meth. **A503**, 513 (2003).

[71] S. Agostinelli et al., Nuclear Instruments and Methods in Physics Research A 506, (2003), p.250.

[72] Geant-4 Physics Reference Manual, http://geant4.cern.ch/support/userdocuments.shtml.

[73] *Applications of the Photonuclear Fragmentation Model to Radiation Protection Problems*, P. V. Degtyarenko, computer code DINREG, Proc. SATIF2, CERN, Oct. 1995

[74] *Modeling single arm electron scattering and nucleon production from nuclei by GeV electrons*, J. W. Lightbody and J. S. O'Connell, Computers in Physics 2, (1988), p.57.

[75] J.J. Kelly, Phys. Rev. C 70, (2004), p.068202.

[76] V. Sapunenko, *et al.*, Nucl. Instr. and Meth. A, to be submitted.

[77] M. Glück, E. Reya, A. Vogt, Z. Phys. C **53**, 651 (1992).

[78] A. D. Martin, R. G. Roberts, W. J. Stirling and P. J. Sutton, Phys. Rev. D **45**, 2349 (1992).